

# Looking for change? Roll the Dice and demand Attention

Foivos I. Diakogiannis<sup>a,b,1</sup>, François Waldner<sup>c</sup>, Peter Caccetta<sup>b</sup>

<sup>a</sup>ICRAR, the University of Western Australia

<sup>b</sup>Data61, CSIRO, Floreat WA

<sup>c</sup>CSIRO Agriculture & Food, St Lucia, QLD, Australia

## Abstract

Change detection, i.e. identification per pixel of changes for some classes of interest from a set of bi-temporal co-registered images, is a fundamental task in the field of remote sensing. It remains challenging due to unrelated forms of change that appear at different times in input images. These are changes due to different environmental conditions or simply changes of objects that are not of interest. Here, we propose a reliable deep learning framework for the task of semantic change detection in very high-resolution aerial images. Our framework consists of a new loss function, new attention modules, new feature extraction building blocks, and a new backbone architecture that is tailored for the task of semantic change detection. Specifically, we define a new form of similarity, that is based on an iterative evaluation of a variant of the Dice coefficient. We use this similarity metric to define a new loss function as well as a new spatial and channel convolution Attention layer (the FracTAL). The new attention layer, designed specifically for vision tasks, is memory efficient, thus suitable for use in all levels of deep convolutional networks. Based on these, we introduce two new efficient self-contained feature extraction convolution units. We term these units CEECNet and FracTAL ResNet units. We validate the performance of these feature extraction building blocks on the CIFAR10 reference data and compare the results with standard ResNet modules. Further, we introduce a new encoder/decoder scheme, a network *macro*-topology, that is tailored for the task of change detection. We validate our approach by showing excellent performance and achieving state of the art score (F1 and Intersection over Union - hereafter IoU) on two building change detection datasets, namely, the LEVIRCD (F1: 0.918, IoU: 0.848) and the WHU (F1: 0.938, IoU: 0.882) datasets.

**Keywords:** convolutional neural network, change detection, Attention, Dice similarity, Tanimoto, semantic segmentation

## 1. Introduction

Change detection is one of the core applications of remote sensing. The goal of change detection is to assign binary labels (“change” or no “change”) to every pixel in a study area based on at least two co-registered images taken at different times. The definition of “change” varies across applications and includes, for instance, urban expansion (Chen and Shi, 2020), flood mapping (Giustarini et al., 2012), deforestation (Morton et al., 2005), and cropland abandonment (Löw et al., 2018). Changes of multiple land-cover classes, i.e. semantic change detection, can also be addressed simultaneously (Daudt et al., 2019). It remains a challenging task due to various forms of change owed to varying environmental conditions that do not constitute a change for the objects of interest (Varghese et al., 2018).

A plethora of change-detection algorithms has been devised and summarised in several reviews (Lu et al., 2004; Coppin et al., 2004; Hussain et al., 2013a; Tewkesbury et al., 2015). In recent years, computer vision has further pushed the state of the art, especially in applications where the spatial context is paramount. The rise of computer vision, especially deep learning, is related to advances and democratisation of powerful computing systems, increasing amounts of available data,

and the development of innovative ways to exploit data (Daudt et al., 2019).

Our starting point is the hypothesis that human intelligence identifies differences in images by looking for change in objects of interest at a higher cognitive level (Varghese et al., 2018). We understand this because the time required for identifying objects that changed between two images, increases with time when the number of changed objects increases (Treisman and Gelade, 1980). That is, there is strong correlation between processing time and number of individual objects that changed. In other words, the higher the complexity of the changes the more time is required to accomplish it. Therefore, simply subtracting extracted features from images (which is a constant time operation) cannot account for the complexities of human perception. As a result, the deep convolutional neural networks proposed in this paper address change detection without using bespoke features subtraction.

In this work, we developed neural networks using attention mechanisms that emphasize areas of interest in two bi-temporal coregistered aerial images. It is the network that learns what to emphasize, and how to extract features that describe change at a higher level. To this end, we propose a dual encoder – single decoder scheme, that fuses information of corresponding layers with relative attention and extracts as a final layer a segmentation mask. This mask designates change for classes of interest,

<sup>1</sup>foivos.diakogiannis@uwa.edu.au



Figure 1: Example of the proposed framework (architecture: mantis CEECNetV1) change detection performance on the LEVIRCD test set (Chen and Shi, 2020). From left to right: input image at date 1, input image at date 2, ground truth buildings change mask, and color coded the true negative (tn), true positive (tp), false positive (fp) and false negative (fn) predictions.

and can also be used for the dual problem of class attribution of change. As in previous work, we facilitate the use of conditioned multi-tasking<sup>2</sup> (Diakogiannis et al., 2020) that proves crucial for stabilizing the training process and improving performance. In summary, the main contributions of this work are:

1. We introduce a new set similarity metric that is a variant of the Dice coefficient, the Fractal Tanimoto similarity measure (section 3). This similarity measure has the advantage that it can be made steeper than the standard Tanimoto metric towards optimality, thus providing a finer-grained similarity metric between layers. The level of steepness is controlled from a depth recursion hyper-parameter. It can be used both as a “sharp” loss function when fine-tuning a model at the latest stages of training, as well as a set similarity metric between feature layers in the attention mechanism.
2. Using the above set similarity as a loss function, we propose an evolving loss strategy for fine-tuning training of neural networks (section 4). This strategy helps to avoid overfitting and improves performance.
3. We introduce the Fractal Tanimoto Attention Layer (hereafter FracTAL), tailored for vision tasks (section 5). This layer uses the fractal Tanimoto similarity to compare queries with keys inside the Attention module. It is a form of spatial and channel attention combined.
4. We introduce a feature extraction building block that is based on the Residual neural network and fractal Tanimoto Attention (section 5.2.1). The new FracTAL ResNet converges faster to optimality than standard residual networks and enhances performance.
5. We introduce two variants of a new feature extraction building block, the Compress-Expand/Expand-Compress unit (hereafter CEECNet unit - section 6.1). This unit exhibits enhanced performance in comparison with standard residual units, and the FracTAL ResNet unit.

<sup>2</sup>The algorithm predicts first the distance transform of the change mask, then it reuses this information and identifies the boundaries of the change mask, and, finally, re-uses both distance transform and boundaries to estimate the change segmentation mask.

6. Capitalizing on these findings, we introduce a new backbone encoder/decoder scheme, a *macro*-topology - the mantis - that is tailored for the task of change detection (section 6.2). The encoder part is a Siamese dual encoder, where the corresponding extracted features at each depth are fused together with FracTAL attention. In this way, information exchange between features extracted from bi-temporal images is enforced. There is no need for manual feature subtraction.
7. Given the relative fusion operation between the encoder features at different levels, our algorithm achieves state of the art performance on the LEVIRCD and WHU datasets without requiring the use of contrastive loss learning during training (section 9). Therefore, it is easier to implement with standard deep learning libraries and tools.

Networks integrating the above-mentioned contributions yielded state of the art performance for the task of building change detection in two benchmark data sets for change detection: the WHU (Ji et al., 2019b) and LEVIRCD (Chen and Shi, 2020) datasets.

In addition to the previously mentioned sections, the following complete the works. In Section 2 we present related work on Attention mechanism and change detection, specialised for the case of very high resolution (hereafter VHR) aerial images. In Section 7 we perform an ablation study of the proposed schemes. In Section 8 we describe the setup of our experiments. Finally, in Section Appendix C we present in MXNET/GLUON style pseudocode various key elements of our architecture<sup>3</sup>.

## 2. Related Work

### 2.1. On attention

The attention mechanism was first introduced by Bahdanau et al. (2014) for the task of neural machine translation<sup>4</sup> (hereafter NMT). This mechanism addressed the problem of translating very long sentences in encoder/decoder architectures. An

<sup>3</sup>A software implementation of the models that relate to this work can be found on <https://github.com/feevos/ceecnet>.

<sup>4</sup>That is, language to language translation of sentences, e.g. English to French.

encoder is a neural network that encodes a phrase to a fixed-length vector. Then the decoder operates on this output and produces a translated phrase (of variable length). It was observed that these types of architectures were not performing well when the input sentences were very long (Cho et al., 2014). The attention mechanism provided a solution to this problem: instead of using all the elements of the encoder vector on equal footing for the decoder, the attention provided a weighted view of them. That is, it emphasized the locations of encoder features that were more important than others for the translation, or stated another way, it emphasized some input words that were more important for the meaning of the phrase. However, in NMT, the location of the translated words is not in direct correspondence with the input phrase, because of the syntax changes. Therefore, Bahdanau et al. (2014) introduced a relative alignment vector,  $e_{ij}$ , that was responsible for encoding the location dependencies: in language, it is not only the meaning (value) of a word that is important but also its relative location in a particular syntax. Hence, the attention mechanism that was devised was comparing the emphasis of inputs at location  $i$  with respect to output words at locations  $j$ . Later, Vaswani et al. (2017) developed further this mechanism and introduced the scaled dot product self-attention mechanism as a fundamental constituent of their Transformer architecture. This allowed the dot product to be used as a similarity measure between feature layers, including feature vectors having large dimensionality.

The idea of using attention for vision tasks soon passed to the community. Hu et al. (2017) introduced channel based attention, in their squeeze and excitation architecture. Wang et al. (2017) used spatial attention to facilitate non-local relationships across sequences of images. Chen et al. (2016) combined both approaches by introducing joint spatial and channel wise attention in convolutional neural networks, demonstrating improved performance on image captioning datasets. To the best of our knowledge, the most faithful implementation of multi-head attention (Vaswani et al., 2017) for convolution layers, is Bello et al. (2019) (spatial attention).

## 2.2. On change detection

Sakurada and Okatani (2015) and Alcantarilla et al. (2016) (see also Guo et al. 2018) were some of the first to introduce fully convolutional networks for the task of scene change detection in computer vision, and they both introduced street view change detection datasets. Sakurada and Okatani (2015) extracted features from a convolutional neural networks and combined them with super pixel segmentation to recover change labels in the original resolution. Alcantarilla et al. (2016) proposed an approach that chains multi-sensor fusion simultaneous localization and mapping (SLAM) with a fast 3D reconstruction pipeline that provides coarsely registered image pairs to an encoder/decoder convolutional network. The output of their algorithm is a pixel-wise change detection binary mask.

Researchers in the field of remote sensing picked up and evolved this knowledge and started using it for the task of land cover change detection. In the remote sensing community, the dual Siamese encoder and a single decoder is frequently adopted.

The majority of different approaches then modifies how the different features extracted from the dual encoder are consumed (or compared) in order to produce a change detection prediction layer. In the following we focus on approaches that follow this paradigm and are most relevant to our work. For a general overview of land cover change detection in the field of remote sensing interested readers can consult Hussain et al. (2013b) and Asokan and Anitha (2019). For a general review on AI applications of change detection to the field of remote sensing Shi et al. (2020).

Caye Daudt et al. (2019) presented and evaluated various strategies for land cover change detection, establishing that their best algorithm was a joint multitasking segmentation and change detection approach. That is, their algorithm predicted simultaneously the semantic classes on each input image, as well as the binary mask of change between the two.

For the task of buildings change detection, Ji et al. (2019a) presented a methodology that is a two-stage process, wherein the first part they use a building extraction algorithm from single date input images. In the second part, the binary masks that are extracted are concatenated together and inserted into a different network that is responsible for identifying changes between the two binary layers. In order to evaluate the impact of the quality of the building extraction networks, the authors use two different architectures. The first, one of the most successful networks to date for instance segmentation, the Mask-RCNN (He et al., 2017), and the second the MS-FCN (multi scale fully convolutional network) that is based on the original UNet architecture (Ronneberger et al., 2015). The advantage of this approach, according to the authors is the fact that they could use unlimited synthetic data for training the second stage of the algorithm.

Chen et al. (2020) used a dual attentive convolutional neural network, i.e. the feature extractor was a siamese VGG16 pre-trained network. The attention module they used for vision, was both spatial and channel attention, and it was the one introduced in Vaswani et al. (2017), however with a single head. Training was performed with a contrastive loss function.

Chen and Shi (2020) presented the STANet, which consists of a feature extractor based on ResNet18 (He et al., 2015), and two versions of spatio-temporal attention modules, the Basic spatial-temporal attention module (BAM) and the pyramid spatial-temporal attention module (PAM). The authors introduced the LEVIRCD change detection dataset and demonstrated excellent performance. Their training process facilitates a contrastive loss applied at the feature pixel level. Their algorithm predicts binary change labels.

Jiang et al. (2020) introduced the PGA-SiamNet that uses a dual Siamese encoder that extracts features from the two input networks. They used VGG16 for feature extraction. A key ingredient to their algorithm is the co-attention module (Lu et al., 2019) that was initially developed for video object segmentation. The authors use it for fusing the extracted features of each input image from the dual VGG16 encoder.



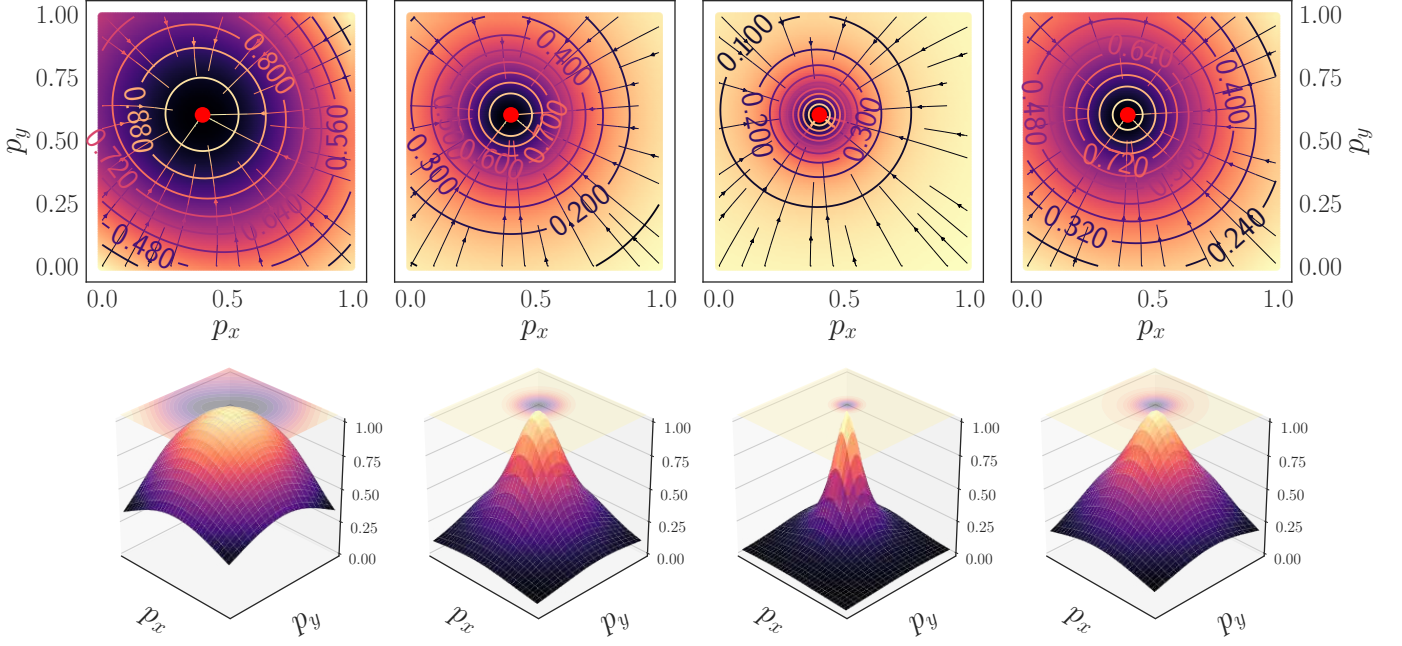


Figure 2: Fractal Tanimoto similarity measure. In the top row we plot the two dimensional density maps for the  $\mathcal{FT}$  similarity coefficient. From left to right the depths are  $d \in \{0, 3, 5\}$ . The last column corresponds to the average of values up to depth  $d = 5$ , i.e.  $\langle \mathcal{FT} \rangle^5 = (1/5) \sum_d \mathcal{FT}^d$ . In the bottom figure we represent in 3D the same values. The horizontal contour plot at  $z = 1$  corresponds to the Laplacian of the  $\mathcal{FT}$ . It is observed that as the depth,  $d$ , of the iteration increases, the function becomes steeper towards optimality.

### 3. Fractal Tanimoto similarity coefficient

In (Diakogiannis et al., 2020) we analyzed the performance of the various flavours of the Dice coefficient and introduced the Tanimoto with complement coefficient. Here, we expand further our analysis, and we present a new functional form for this similarity metric. We use it both as a self-similarity measure between convolution layers in a new attention module, as well as a loss function for finetuning semantic segmentation models.

For two (fuzzy) binary vectors of equal dimension,  $\mathbf{p}, \mathbf{l}$ , whose elements lie in the range  $[0, 1]$  the Tanimoto similarity coefficient is defined:

$$T(\mathbf{p}, \mathbf{l}) = \frac{\mathbf{p} \cdot \mathbf{l}}{\mathbf{p}^2 + \mathbf{l}^2 - \mathbf{p} \cdot \mathbf{l}} \quad (1)$$

Interestingly, the dot product between two fuzzy binary vectors is another similarity measure of their agreement. This inspired us to introduce an iterative functional form of the Tanimoto:

$$\mathcal{T}^0 \equiv T(\mathbf{p}, \mathbf{l}) = \frac{\mathbf{p} \cdot \mathbf{l}}{\mathbf{p}^2 + \mathbf{l}^2 - \mathbf{p} \cdot \mathbf{l}} \quad (2)$$

$$\mathcal{T}^d = \frac{\mathcal{T}^{d-1}(\mathbf{p}, \mathbf{l})}{\mathcal{T}^{d-1}(\mathbf{p}, \mathbf{p}) + \mathcal{T}^{d-1}(\mathbf{l}, \mathbf{l}) - \mathcal{T}^{d-1}(\mathbf{p}, \mathbf{l})} \quad (3)$$

For example, expanding Eq. (2) for  $d = 3$ , yields:

$$\mathcal{T}^3(\mathbf{p}, \mathbf{l}) = \frac{\mathbf{p} \cdot \mathbf{l}}{(\mathbf{l}^2 - \mathbf{p} \cdot \mathbf{l} + \mathbf{p}^2) \left( 2 - \frac{\mathbf{p} \cdot \mathbf{l}}{\mathbf{l}^2 - \mathbf{p} \cdot \mathbf{l} + \mathbf{p}^2} \right) \left( 2 - \frac{\mathbf{p} \cdot \mathbf{l}}{(\mathbf{l}^2 - \mathbf{p} \cdot \mathbf{l} + \mathbf{p}^2) \left( 2 - \frac{\mathbf{p} \cdot \mathbf{l}}{\mathbf{l}^2 - \mathbf{p} \cdot \mathbf{l} + \mathbf{p}^2} \right)} \right)} \quad (4)$$

We can expand this for an arbitrary depth  $d$  and then we get the following simplified version<sup>5</sup> of the fractal Tanimoto similarity measure:

$$\mathcal{T}^d(\mathbf{p}, \mathbf{l}) = \frac{\mathbf{p} \cdot \mathbf{l}}{2^d(\mathbf{p}^2 + \mathbf{l}^2) - (2^{d+1} - 1)\mathbf{p} \cdot \mathbf{l}} \quad (5)$$

This function takes values in the range  $[0, 1]$  and it becomes steeper as  $d$  increases. At the limit  $d \rightarrow \infty$  it behaves like the integral of the Dirac  $\delta$  function around point  $\mathbf{l}$ ,  $\int \delta(\mathbf{p} - \mathbf{l}) d\mathbf{p}$ . That is, the parameter  $d$  is a form of annealing “temperature”. Interestingly, although the iterative scheme was defined with  $d$  being an integer, for continuous values  $d \geq 0$ ,  $\mathcal{T}^d$  remains bounded in the interval  $[0, 1]$ . That is:

$$\mathcal{T}^d : \mathcal{R}^n \times \mathcal{R}^n \rightarrow U \subseteq [0, 1] \quad (6)$$

where  $n = \dim(\mathbf{p})$  is the dimensionality of the fuzzy binary vectors  $\mathbf{p}, \mathbf{l}$ .

In the following we will use the functional form of the fractal Tanimoto with complement (Diakogiannis et al., 2020), i.e.:

$$\mathcal{FT}^d(\mathbf{p}, \mathbf{l}) \equiv \frac{\mathcal{T}^d(\mathbf{p}, \mathbf{l}) + \mathcal{T}^d(\mathbf{1} - \mathbf{p}, \mathbf{1} - \mathbf{l})}{2} \quad (7)$$

In Fig. 2 we provide a simple example for a ground truth vector  $\mathbf{l} = \{0.4, 0.6\}$  and a continuous vector of probabilities  $\mathbf{p} = \{p_x, p_y\}$ . On the top panel, we construct density plots of the Fractal Tanimoto function with complement,  $\mathcal{FT}^d$ . Overplotted

<sup>5</sup>The simplified formula was obtained with MATHEMATICA 11 Software.

are the gradient field lines that point to the ground truth. In the bottom pannels, we plot the corresponding 3D representations. From left to right, the first column corresponds to  $d = 0$ , the second to  $d = 3$  and the third to  $d = 5$ . It is apparent that the effect of the  $d$  hyperparameter is to make the similarity metric steeper towards the ground truth. For all practical purposes (network architecture, evolving loss function) we use the average fractal Tanimoto loss (last column), due to having steeper gradients away from optimality:

$$\langle \mathcal{FT} \rangle^d(\mathbf{p}, \mathbf{l}) \equiv \frac{1}{d} \sum_{i=0}^{d-1} \mathcal{FT}^i(\mathbf{p}, \mathbf{l}) \quad (8)$$

#### 4. Evolving loss strategy

In this section, we describe a training strategy that modifies the depth of the fractal Tanimoto similarity coefficient, when used as a loss function, on each learning rate reduction. For minimization problems, the fractal Tanimoto loss is defined through:  $L = 1 - \langle \mathcal{FT} \rangle^d$ . In the following, when we refer to the fractal Tanimoto loss function, it should be understood that this is defined through the similarity coefficient, as described above.

During training, and until the first learning rate reduction we use the standard Tanimoto with dual  $\mathcal{FT}^0(\mathbf{p}, \mathbf{l})$ . The reason for this is that for a random initialization of the weights (i.e. for an initial prediction point in the space of probabilities away from optimality), the gradients are steeper towards the best values for this particular loss function (in fact, for cross entropy are even steeper). This can be seen in Fig. 2 in the bottom row: clearly for an initial probability vector  $\mathbf{p} = \{p_x, p_y\}$  away from the ground truth  $\mathbf{l} = \{0.4, 0.6\}$  the gradients are steeper for  $d = 0$ . As training evolves, and the value of the weights approaches optimality, the predictions approach the ground truth and the loss function flattens out. With batch gradient descent (and variants), we are not really calculating the true (global) loss function, but a noisy approximate version of it. This is because in each batch loss evaluation, we are not using all of the data for the gradients evaluation. In Fig. 3 we represent a graphical representation of the true landscape and a noisy version of it for a toy 2D problem. In the top row, we plot the value of the  $\mathcal{FT}^0$  similarity as well as the average value of the loss functions for  $d = 0, \dots, 9$  for the ground truth vector  $\mathbf{l} = \{0.4, 0.6\}$ . In the corresponding bottom rows, we have the same plot were we also added random Gaussian noise. In the initial phases of training, the average gradients are greater than the local values dues to noise. As the network reaches optimality the average gradient towards optimality becomes smaller and smaller, and the gradients due to noise dominate the training. Once we reduce the learning rate, the step the optimizer takes is even smaller, therefore it cannot easily escape local optima (due to noise). What we propose is to “shift gears”: once training stagnates, we change the loss function to a similar but steeper one towards optimality that can provide gradients (on average) that can dominate the noise. Our choice during training is the following set of learning rates and depths of the fractal Tanimoto loss:  $\{(1\text{r} : 10^{-3}, d = 0), (1\text{r} : 10^{-4}, d = 10), (1\text{r} : 10^{-5}, d = 20)\}$ .

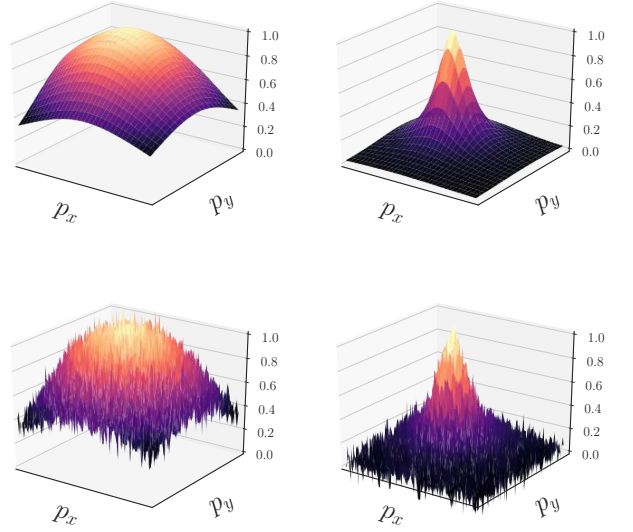


Figure 3: Fractal Tanimoto similarity measure with noise. On the top row, from left to right is the  $\mathcal{FT}^1(\mathbf{p}, \mathbf{l})$  and  $(1/10) \sum_{d=0}^9 (\mathcal{FT}^d(\mathbf{p}, \mathbf{l}))$ . The bottom row is the same corresponding  $\mathcal{FT}^d(\mathbf{p}, \mathbf{l})$  similarity measures, with Gaussian random noise added. When the algorithmic training approaches optimality with the standard Tanimoto, local noise gradients tend to dominate over the background average gradient. Increasing the slope of the background gradient at later stages of training is a remedy to this problem.

In all evaluations of loss functions for  $d > 0$ , we use the average value for all  $d$  values (Eq. 8).

#### 5. Fractal Tanimoto Attention

Here, we present a novel convolutional attention layer based on the new similarity metric and a methodology of fusing information from the output of the attention layer to features extracted from convolutions.

##### 5.1. Fractal Tanimoto Attention layer

In the pioneering work of Vaswani et al. (2017) the attention operator is defined through a scaled dot product operation. For images in particular, i.e. two dimensional features, assuming that  $\mathbf{q} \in \mathbb{R}^{C_q \times H \times W}$  is the query,  $\mathbf{k} \in \mathbb{R}^{C \times H \times W}$  the key and  $\mathbf{v} \in \mathbb{R}^{C \times H \times W}$  it's corresponding value, the (spatial) attention is defined as (see also Zhang et al. 2020):

$$\mathbf{o} = \text{softmax} \left( \frac{\mathbf{q} \circ_1 \mathbf{k}}{\sqrt{d}} \right), \quad \in \mathbb{R}^{C_q \times C} \quad (9)$$

$$\text{Att}(\mathbf{q}, \mathbf{k}, \mathbf{v}) = \mathbf{o} \circ_2 \mathbf{v}, \quad \in \mathbb{R}^{C_q \times H \times W} \quad (10)$$

Here  $d$  is the dimension of the keys and the softmax operation is with respect to the first (channel) dimension. The term  $\sqrt{d}$  is a scaling factor that ensures the Attention layer scales well even with a large number of dimensions (Vaswani et al., 2017). The operator  $\circ_1$  corresponds to inner product with respect to the spatial dimensions height,  $H$ , and width,  $W$ , while  $\circ_2$  is a dot

product with respect to channel dimensions<sup>6</sup>. In this formalism each channel of the query features is compared with each of the channels of the key values. In addition there is a 1 – 1 correspondence between keys and values, meaning that for each key corresponds a unique value. The point of the dot product is to emphasize the key-value pairs that are more relevant for the particular query. That is the dot product selects the keys that are most similar to the particular query. It represents the projection of queries on the keys space. The softmax operator provides a weighted “view” of all the values for a particular set of queries, keys and values- or else a “soft” attention mechanism. In the multi-head attention paradigm, multiple attention heads that follow the principles described above are concatenated together. One of the key disadvantages of this formulation when used in vision tasks (i.e. two dimensional features) is the very large memory footprint that this layer exhibits. For 1D problems, such as Natural Language Processing, this is not - in general - an issue.

Here we follow a different approach. We develop our formalism for the case where the number of query channels,  $C_q$  is identical to the number of key channels,  $C$ . However, if desired, our formalism can work for the general case where  $C_q \neq C$ .

Let  $\mathbf{q} \in \mathbb{R}^{C \times H \times W}$  be the query features,  $\mathbf{k} \in \mathbb{R}^{C \times H \times W}$  the keys and  $\mathbf{v} \in \mathbb{R}^{C \times H \times W}$  the values. In our formalism, it is a requirement for these operators to have values in  $[0, 1]$ <sup>7</sup>. Our approach is a joint spatial and channel attention mechanism. With the use of the Fractal Tanimoto similarity coefficient, we define the *spatial*,  $\boxtimes$ , and *channel*,  $\boxdot$ , similarity between the query,  $\mathbf{q}$ , and key,  $\mathbf{k}$ , features according to:

$$\mathcal{T}_{\boxtimes}^d(\mathbf{q}, \mathbf{k}) = \frac{\mathbf{q} \boxtimes \mathbf{k}}{2^d (\mathbf{q} \boxtimes \mathbf{q} + \mathbf{k} \boxtimes \mathbf{k}) - (2^{d+1} - 1) \mathbf{q} \boxtimes \mathbf{k}} \in \mathbb{R}^C \quad (11)$$

$$\mathcal{T}_{\boxdot}^d(\mathbf{q}, \mathbf{k}) = \frac{\mathbf{q} \boxdot \mathbf{k}}{2^d (\mathbf{q} \boxdot \mathbf{q} + \mathbf{k} \boxdot \mathbf{k}) - (2^{d+1} - 1) \mathbf{q} \boxdot \mathbf{k}} \in \mathbb{R}^{H \times W} \quad (12)$$

where the spatial and channel products are defined as:

$$\begin{aligned} \mathbf{q} \boxtimes \mathbf{k} &= \sum_{jk} q_{ijk} k_{ijk} \in \mathbb{R}^C \\ \mathbf{q} \boxdot \mathbf{k} &= \sum_i q_{ijk} k_{ijk} \in \mathbb{R}^{H \times W} \end{aligned}$$

It is important to note that the output of these operators lies numerically within the range  $[0, 1]$ , where 1 indicates identical similarity and 0 indicates no correlation between the query and key. That is, there is no need for normalization or scaling as is the case for the traditional dot product similarity.

<sup>6</sup>This is more apparent in index notation:

$$\begin{aligned} \mathbf{q} \circ_1 \mathbf{k} &\equiv \sum_{jk} q_{ijk} k_{ijk} \in \mathbb{R}^{C_q \times C} \\ \mathbf{o} &\equiv \text{softmax}(\mathbf{q} \circ_1 \mathbf{k}) \equiv \mathbf{o}_{il} \\ \text{Att}(\mathbf{q}, \mathbf{k}, \mathbf{v}) &\equiv \text{Att}_{ijk} \equiv \mathbf{o} \circ_2 \mathbf{v} \equiv \sum_l \mathbf{o}_{il} v_{lkj} \in \mathbb{R}^{C_q \times H \times W} \end{aligned}$$

<sup>7</sup>This can be easily achieved by applying the sigmoid operator.

In our approach the spatial and channel attention layers are defined with element-wise multiplication<sup>8</sup> (denoted by the symbol  $\odot$ ):

$$\text{Att}_{\boxtimes}(\mathbf{q}, \mathbf{k}, \mathbf{v}) = \mathcal{T}_{\boxtimes}^d(\mathbf{q}, \mathbf{k}) \odot \mathbf{v}$$

$$\text{Att}_{\boxdot}(\mathbf{q}, \mathbf{k}, \mathbf{v}) = \mathcal{T}_{\boxdot}^d(\mathbf{q}, \mathbf{k}) \odot \mathbf{v}$$

It should be stressed that these operations do not consider that there is a 1 – 1 mapping between keys and values. Instead, we consider a map of one-to-many, that is a single key can correspond to a set of values. Therefore, there is no need to use a softmax activation (see also Kim et al. 2017). The overall attention is defined as the average of the sum of these two operators:

$$\text{Att}(\mathbf{q}, \mathbf{k}, \mathbf{v}) = 0.5(\text{Att}_{\boxtimes} + \text{Att}_{\boxdot}) \quad (13)$$

In practice we use the averaged fractal Tanimoto similarity coefficient with dual,  $\langle \mathcal{FT} \rangle_{\boxtimes/\boxdot}^d$ , both for spatial and channel wise attention.

As stated previously, it is possible to extend the definitions of spatial and channel products in a way where we compare each of the channels (respectively, spatial pixels) of the query with each of the channels (respectively, spatial pixels) of the key. However, this imposes a heavy memory footprint, and makes deeper models, even for modern-day GPUs, prohibitive. In addition, we found that this approach did not improve performance for the case of change detection and classification. Indeed, one needs to question this for vision tasks: the initial definition of attention (Bahdanau et al., 2014) introduced a relative alignment vector,  $e_{ij}$ , that was necessary because, for the task of NMT, the syntax of phrases changes from one language to the other. That is, the relative emphasis with respect to location between two vectors is meaningful. When we compare two images (features) at the same depth of a network (created by two different inputs, as is the case for change detection), we anticipate that the channels (or spatial pixels) will be in correspondence. For example, the RGB (or hyperspectral) order of inputs, does not change. That is, in vision, the situation can be different than NLP because we do not have a relative location change as it happens with words in phrases.

We propose the use of the Fractal Tanimoto Attention Layer (hereafter FracTAL) for vision tasks as an improvement over the scaled dot product attention mechanism (Vaswani et al., 2017) for the following reasons:

1. The  $\mathcal{FT}$  similarity is automatically scaled in the region  $[0, 1]$ , therefore it does not require normalization, or activation to be applied. This simplifies the design and implementation of Attention layers and enables training without ad-hoc normalization operations.
2. The dot product does not have an upper or lower bound, therefore a positive value cannot be a quantified measure of similarity. In contrast  $\mathcal{FT}$  has a bounded range of values in  $[0, 1]$ . The lowest value indicates no correlation, and the maximum value perfect similarity. It is thus easier to interpret.

<sup>8</sup>We use PYTHON NUMPY (Oliphant, 2006) semantics of broadcasting since the dimensions do not match.

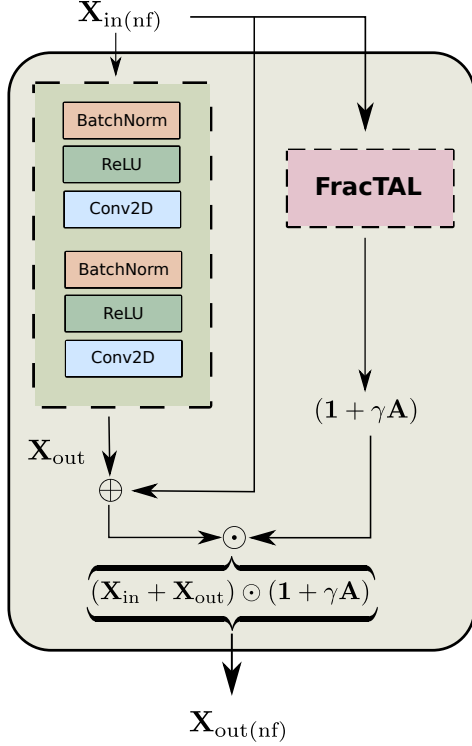


Figure 4: The FracTAL Residual unit. This building block demonstrates the fusion of the residual block with self FracTAL evaluated from the input features.

3. Iteration  $d$  is a form of hyperparameter, like “temperature” in annealing. Therefore, the  $\mathcal{FT}$  can become as steep as we desire (by modification of the temperature parameter  $d$ ), steeper than the dot product similarity. This can translate to finer query and key similarity.
4. Finally, it is efficient in terms of GPU memory footprint (when one considers that it does both channel and spatial attention), thus allowing the design of more complex convolution building blocks.

The implementation of the FracTAL is given in Listing 2. The multihead attention is achieved using group convolutions for the evaluation of queries, keys and values.

## 5.2. Attention fusion

A critical part in the design of convolution building blocks enhanced with attention is the way the information from attention is passed to convolution layers. To this aim we propose fusion methodologies of feature layers with the FracTAL for two cases: self attention fusion, and a relative attention fusion where information from two layers are combined.

### 5.2.1. Self attention fusion

We propose the following fusion methodology between a feature layer,  $\mathbf{L}$ , and its corresponding FracTAL self-attention layer,  $\mathbf{A}$ :

$$\mathbf{F} = \mathbf{L} + \gamma \mathbf{L} \odot \mathbf{A} = \mathbf{L} \odot (\mathbf{1} + \gamma \mathbf{A}) \quad (14)$$

Here  $\mathbf{F}$  is the output layer produced from the fusion of  $\mathbf{L}$  and the Attention layer,  $\mathbf{A}$ ,  $\odot$  describes element wise multiplication,

$\mathbf{1}$  is a layer of ones like  $\mathbf{L}$ , and  $\gamma$  a trainable parameter initiated at zero. We next describe the reasons why we propose this type of fusion.

The Attention output is maximal (i.e. close to 1) in areas on the features where it must “attend” and minimal otherwise (i.e. close to zero). Multiplying element-wise directly the FracTAL attention layer  $\mathbf{A}$  with the features,  $\mathbf{L}$ , effectively lowers the values of features in areas that are not “interesting”. It does not alter the value of areas that “are interesting”. This can produce loss of information in areas where  $\mathbf{A}$  “does not attend” (i.e. it does not emphasize), that would be otherwise valuable at a later stage. Indeed, areas of the image that the algorithm “does not attend” should not be perceived as empty space (Treisman and Gelade, 1980). For this reason the “emphasized” features,  $\mathbf{L} \odot \mathbf{A}$  are added to the original input  $\mathbf{L}$ . That is  $\mathbf{L} + \mathbf{L} \odot \mathbf{A}$  is identical to  $\mathbf{L}$  in spatial areas where  $\mathbf{A}$  tends to zero, and is emphasized in areas where  $\mathbf{A}$  is maximal.

In the initial stages of training, the attention layer,  $\mathbf{A}$ , does not contribute to  $\mathbf{L}$ , due to the initial value of the trainable parameter  $\gamma_0 = 0$ . Therefore it does not add complexity during the initial phase of training and it allows for an annealing process of Attention contribution (Zhang et al., 2018, see also Chen et al. 2020). This property is particularly important when  $\mathbf{L}$  is produced from a known performant recipe (e.g. residual building blocks).

In Fig 4 we present this fusion mechanism for the case of a Residual unit (He et al., 2016, 2015). Here the input layer,  $\mathbf{X}_{in}$ , is subject to the residual block sequence of Batch normalization, convolutions, and ReLU activations, and produces the  $\mathbf{X}_{out}$  layer. A separate branch uses the  $\mathbf{X}_{in}$  input to produce the self attention layer  $\mathbf{A}$  (see Listing 2). Then we multiply element wise the standard output of the residual unit,  $\mathbf{X}_{in} + \mathbf{X}_{out}$ , with the  $\mathbf{1} + \gamma \mathbf{A}$  layer. In this way, at the beginning of training, this layer behaves as a residual layer, which has the excellent convergent properties of resnet at initial stages, and at later stages of training the Attention becomes gradually more active and allows for greater performance. A software routine of this fusion for the residual unit, in particular, can be seen in Listing 4 in the Appendix.

### 5.2.2. Relative attention fusion

Assuming we have two input layers,  $\mathbf{L}_1, \mathbf{L}_2$ , we can calculate the relative attention of each with respect to the other. This is achieved by using as query the layer we want to “attend to” and as a key and value the layer we want to use as information for attention. In practical implementations, the query, the key, and the value layers result in after the application of a convolution layer to some input.

$$\mathbf{F}_1 = \mathbf{L}_1 \odot [\mathbf{1} + \gamma_1 \mathbf{A}_{122}(\mathbf{q}(\mathbf{L}_1), \mathbf{k}(\mathbf{L}_2), \mathbf{v}(\mathbf{L}_2))] \quad (15)$$

$$\mathbf{F}_2 = \mathbf{L}_2 \odot [\mathbf{1} + \gamma_2 \mathbf{A}_{211}(\mathbf{q}(\mathbf{L}_2), \mathbf{k}(\mathbf{L}_1), \mathbf{v}(\mathbf{L}_1))] \quad (16)$$

$$\mathbf{F} = \text{Conv2DN}(\text{concat}([\mathbf{F}_1, \mathbf{F}_2])) \quad (17)$$

Here, the  $\gamma_{1,2}$  parameters are initialized at zero, and the concatenation operations are performed along the channel dimension. Conv2DN is a two dimensional convolution operation followed by a normalization layer, e.g. BatchNorm (Ioffe and Szegedy,



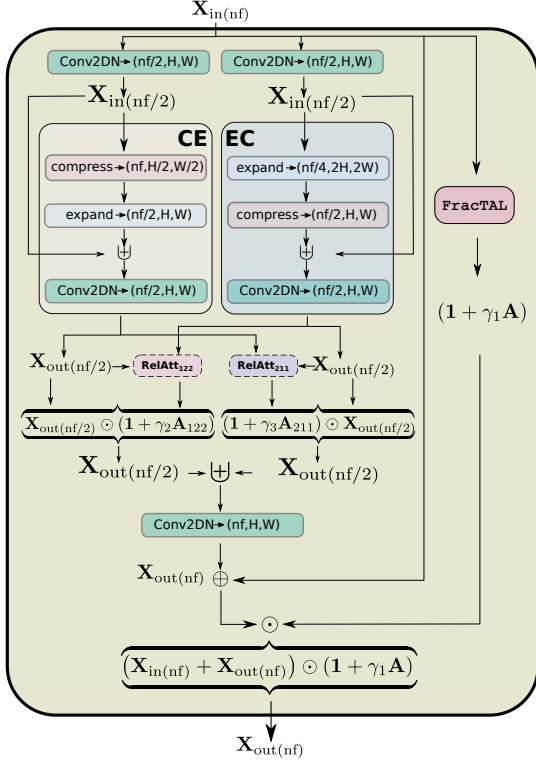


Figure 5: Compress Expand Expand Compress unit (CEECNet). The symbol  $\oplus$  represents concatenation of features along the channel dimension (for V1). For version V2, we replace the concatenation,  $\oplus$  followed by the normalized convolution layer with a relative fusion attention, as described in Section 5.2.2

2015)). An implementation of this process in MXNET/GLUON pseudocode style can be found in Listing 3.

The relative attention fusion presented here can be used as a direct replacement of concatenation followed by a convolution layer in any network design.

## 6. Architecture

We break down the network architecture into three component parts: the *micro*-topology of the building blocks, which represents the fundamental constituents of the architecture; the *macro*-topology of the network, which describes how building blocks are connected to one another to maximize performance; and the multitasking head, which is responsible for transforming the features produced by the micro and macro-topologies into the final prediction layers where change is identified. Each of the choices of micro and macro topology has a different impact on the GPU memory footprint. Usually, selecting very deep macro-topology improves performance, but then this increases the overall memory footprint and does not leave enough space for using an adequate number of filters (channels) in each micro-topology. There is obviously a trade off between the micro-topology feature extraction capacity and overall network depth. Guided by this, we seek to maximize the feature expression capacity of the micro-topology for a given number of filters, perhaps at the expense of consuming computational resources.

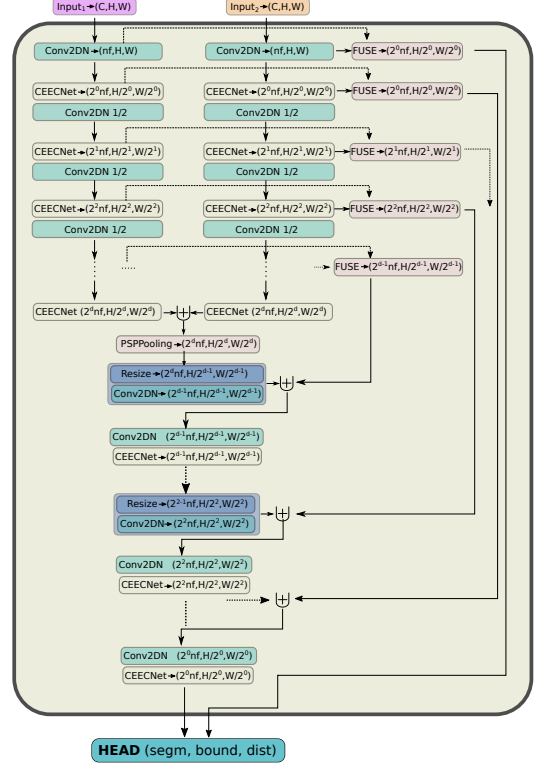


Figure 6: The mantis CEECNetV1 architecture for the task of change detection. The Fusion operation (FUSE) is described with MXNET/GLUON style pseudocode in detail on Listing 3.

### 6.1. Micro-topology: the CEECNet unit

The basic intuition behind the construction of the CEEC building block, is that it provides two different, yet complementary, views for the same input. The first view (the **CE** block - see Fig. 5) is a “summary understanding” operation (performed in lower resolution than the input - see also Newell et al. 2016; Liu et al. 2020 and Qin et al. 2020). The second view (the **EC** block) is an “analysis of detail” operation (performed in higher spatial resolution than the input). It then exchanges information between these two views using relative attention, and it finally fuses them together, by emphasizing the most important parts using the Fractal .

Our hypothesis and motivation for this approach is quite similar to the scale-space analysis in computer vision (Lindeberg, 1994): viewing input features at different scales, allows the algorithm to focus on different aspects of the inputs, and thus perform more efficiently. The fact that by merely increasing the resolution of an image does not increase its content information is not relevant here: guided by the loss function the algorithm can learn to represent at higher resolution features that otherwise would not be possible in lower resolutions. We know this from the successful application of convolutional networks in super-resolution problems (Wang et al., 2019) as well as (variational) autoencoders (Tschannen et al., 2018; Kingma and Welling, 2019): in both of these paradigms deep learning approaches manage to increase meaningfully the resolution of features that exists in lower spatial dimension layers.



In the following we define the volume  $V$  of features of dimension  $(C, H, W)$ <sup>9</sup>, as the product of the number of their channels (or filters),  $C$  (or  $nf$ ), with their spatial dimensions, height,  $H$ , and width,  $W$ , i.e.  $V = nf \cdot H \cdot W$ <sup>10</sup>. The two branches consist of: a “mini U-Net” operation (CE block), that is responsible for summarizing information from the input features by first compressing the total volume of features into half its original size and then restoring it. The second branch, a “mini  $\cap$ -Net” operation (EC block), is responsible for analyzing in higher detail the input features: it initially doubles the volume of the input features, by halving the number of features and doubling each spatial dimension. It subsequently compresses this expanded volume to its original size. The input to both layers is concatenated with the output, and then a normed convolution restores the number of channels to their original input value. Note that the mini  $\cap$ -Net is nothing more than the symmetric (or dual) operation of the mini U-Net.

The outputs of the EC and CE blocks are fused together with relative attention fusion (section 5.2.2). In this way, exchange of information between the layers is encouraged. The final emphasized outputs are concatenated together, thus restoring the initial number of filters, and the produced layer is passed through a normed convolution in order to bind the relative channels. The operation is concluded with a FracTAL residual operation and fusion (similar to Fig. 4), where the input is added to the final output and emphasized by the self attention on the original input. The CEECNet building block is described schematically in Fig. 5.

The compression operation, **C**, is achieved by applying a normed convolution layer of stride equal to 2 ( $k=3, p=1, s=2$ ) followed by another convolution layer that is identical in every aspect except the stride that is now  $s=1$ . The purpose of the first convolution is to both resize the layer and extract features. The purpose of the second convolution layer is to extract features. The expansion operation, **E**, is achieved by first resizing the spatial dimensions of the input layer using Bilinear interpolation, and then the number of channels is brought to the desired size by the application of a convolution layer ( $k=3, p=1, s=1$ ). Another identical convolution layer is applied to extract further features. The full details of the convolution operations used in the EC and CE blocks can be found on Listing 5.

## 6.2. Macro-topology: dual encoder, symmetric decoder

In this section we present the macro-topology (i.e. backbone) of the architecture that uses as building blocks either the CEECNet or the FracTAL ResNet units. We start by stating the intuition behind our choices and continue with a detailed description of the macro-topology. Our architecture is heavily influenced from the ResUNet—a model (Diakogiannis et al., 2020). We will refer to this macro-topology as the *mantis* topology<sup>11</sup>.

<sup>9</sup>Here,  $C$  is the number of channels,  $H$  and  $W$  the spatial dimensions, height and width respectively.

<sup>10</sup>For example, for each batch dimension, the output volume of a layer of size  $(C, H, W) = (32, 256, 256)$  is  $V = 32 \cdot 256^2 = 2097152$ .

<sup>11</sup>For no particular reason, other than that the *mantis* shrimp is an [amazing sea creature](#) that resides in the waters of Australia.

In designing this backbone, a key question we tried to address is how can we facilitate exchange of information between features extracted from images at different dates. The following two observations guided us:

1. We make the hypothesis that the process of change detection between two images requires a mechanism similar to human attention. We base this hypothesis on the fact that the time required for identifying objects that changed in an image correlates directly with the number of changed objects. That is, the more objects a human needs to identify between two pictures, the more time is required. This is in accordance with the feature-integration theory of Attention (Treisman and Gelade, 1980). In contrast, subtracting features extracted from two different input images is a process that is constant in time, independent of the complexity of the changed features. Therefore, we avoid using adhoc feature subtraction in all parts of the network.
2. In order to identify change, a human needs to look and compare two images multiple times, back and forth. We need *things to emphasize on image at date 1, based on information on image at date 2* (Eq. 15), and, vice versa (Eq. 16). And then combine both of these information together (Eq. 17). That is, exchange information, with relative attention (section 5.2.2) between the two, at multiple levels. A different way of stating this as a question is: what is *important* on input image 1 based on *information* that exists on image 2, and vice versa?

Given the above, we now proceed in detailing the *mantis* macro-topology (with CEECNetV1 building blocks, see Fig. 6). The encoder part is a series of building blocks, where the size of the features is downscaled between the application of each subsequent building block. Downscaling is achieved with a normed convolution with stride,  $s=2$  without using activations. There exist two encoder branches that share identical parameters in their convolution layers. The input to each branch is an image from a different date and the role of the encoder is to extract features at different levels from each input image. During the feature extraction by each branch, each of the two inputs is treated as an independent entity. At successive depths, the outputs of the corresponding building block are fused together with the relative attention methodology as described in section 5.2.2, but they are not used until later, in the decoder part. Crucially, this fusion operation, suggests to the network that the *important parts of the first layer, will be defined by what exists on the second layer* (and vice versa), but it does not dictate how exactly the network should compare the extracted features (e.g. by demanding the features to be similar for unchanged areas, and maximally different for changed areas<sup>12</sup>). This is something that the network will have to discover in order to match its predictions with the ground truth. Finally, the last encoder layers are concatenated and inserted to the pyramid scene pooling layer (PSPPooling – Diakogiannis et al. 2020; Zhao et al. 2017).

<sup>12</sup>We tried this approach and it was not successful.

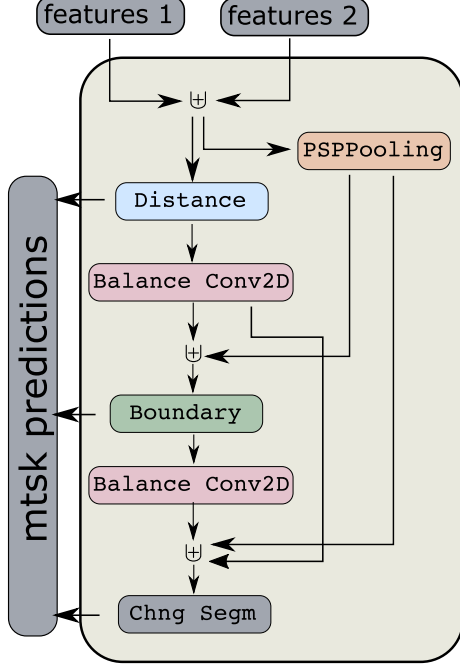


Figure 7: Conditioned multitasking segmentation HEAD. Here, features 1 and 2 are the outputs of the *mantis* CEECNet features extractor. The symbol  $\oplus$  represents concatenation along the channels dimension. The algorithm first predicts the distance transform of the classes (regression), then re-uses this information to estimate the boundaries and finally both of these predictions are re-used for the change prediction layer.

In the (single) decoder part is where the network extracts features based on the relative information that exist in the two inputs. Starting from the output of the PSPPooling layer (middle of network), we upscale lower resolution features with bilinear interpolation and combine them with the fused outputs of the decoder with a concatenation operation followed by a normed convolution layer, in a way similar to the ResUNet-a (Diakogiannis et al., 2020) model. The *mantis* CEECNetV2 model replaces all concatenation operations followed by a normed convolution, with a Fusion operation as described in Listing 3.

The final features extracted from this macro-topology architecture is the final layer from the CEECNet unit that has the same spatial dimensions as the first input layers, as well as the Fused layers from the *first* CEECNet unit operation. Both of these layers are inserted in the segmentation HEAD.

### 6.3. Segmentation HEAD

The features extracted from the features extractor (Fig. 6) are inserted to a conditioned multitasking segmentation head (Fig. 7) that produces three layers: a segmentation mask, a boundary mask and a distance transform mask. This is identical with the ResUNet-a “causal” segmentation head, that has shown great performance in a variety of segmentation tasks (Diakogiannis et al., 2020; Waldner and Diakogiannis, 2020), with two modifications.

The first modification relates to the evaluation of boundaries: instead of using a standard sigmoid activation for the boundaries layer, we are inserting a scaling parameter,  $\gamma$ , that

controls how sharp the transition from 0 to 1 takes place, i.e.

$$\text{sigmoid}_{\text{crisp}}(x) = \text{sigmoid}(x/\gamma), \quad \gamma \in [\epsilon, 1] \quad (18)$$

Here  $\epsilon = 10^{-2}$  is a smoothing parameter. The  $\gamma$  coefficient is learned during training. We inserted this scaling after noticing in initial experiments that the algorithm needed improvement close to the boundaries of objects. In other words, the algorithm was having difficulty separating nearby pixels. Numerically, we anticipate that the distance between the values of activations of neighbouring pixels is small, due to the patch-wise nature of convolutions. Therefore, a remedy to this problem is making the transition boundary sharper. We initialize training with  $\gamma = 1$ .

The second modification to the segmentation HEAD relates to balancing the number of channels of the boundaries and distance transform predictions before re-using them in the final prediction of segmentation change detection. This is achieved by passing them through a convolution layer that brings the number of channels to the desired number. Balancing the number of channels treats the input features and the intermediate predictions as equal contributions to the final output. In Fig. 7 we present schematically the conditioned multitasking head, and the various dependencies between layers. Interested users can refer to Diakogiannis et al. (2020) for details of the conditioned multitasking head.

## 7. FracTAL units and evolving loss ablation study

In this section we present the performance of the FracTAL ResNet and CEECNet units we introduced as well as the effect of the evolving  $\langle \mathcal{FT} \rangle^d$  loss function on training a neural network.

### 7.1. FracTAL building blocks performance

We construct three identical networks in macro-topological graph (backbone), but different in micro-topology (building blocks). The first two networks are equipped with two different versions of CEECNet: the first is identical with the one presented in Fig. 5. The second is similar to the one in Fig. 5 with all concatenation operations that are followed by normed convolutions being replaced with Fusion operations, as described in Listing 3. The third network uses as building blocks the FracTAL ResNet building blocks (Fig. 4). Finally, the fourth network uses as building blocks standard residual units as described in He et al. (2016, 2015) (ResNet V2). All building blocks have the same dimensionality of input and output features. However, each type of building block has a different number of parameters. By keeping the dimensionality of input and output layers identical to all layers, we believe, the performance differences of the networks will reflect the feature expression capabilities of the building blocks we compare.

In Fig. 8 we plot the validation loss for 300 epochs of training on CIFAR10 dataset (Krizhevsky, 2009) without learning rate reduction, We use cross entropy loss and Adam optimizer

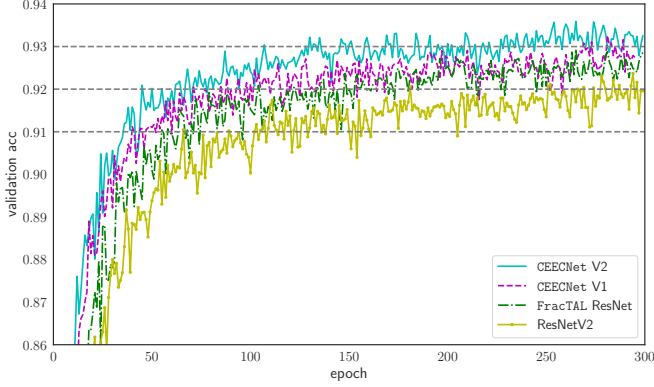


Figure 8: Comparison of the V1 and V2 versions of CEECNet building blocks with a FracTAL ResNet implementation and a standard ResNet V2 building blocks. The models were trained for 300 epochs on CIFAR10 with standard cross entropy loss.

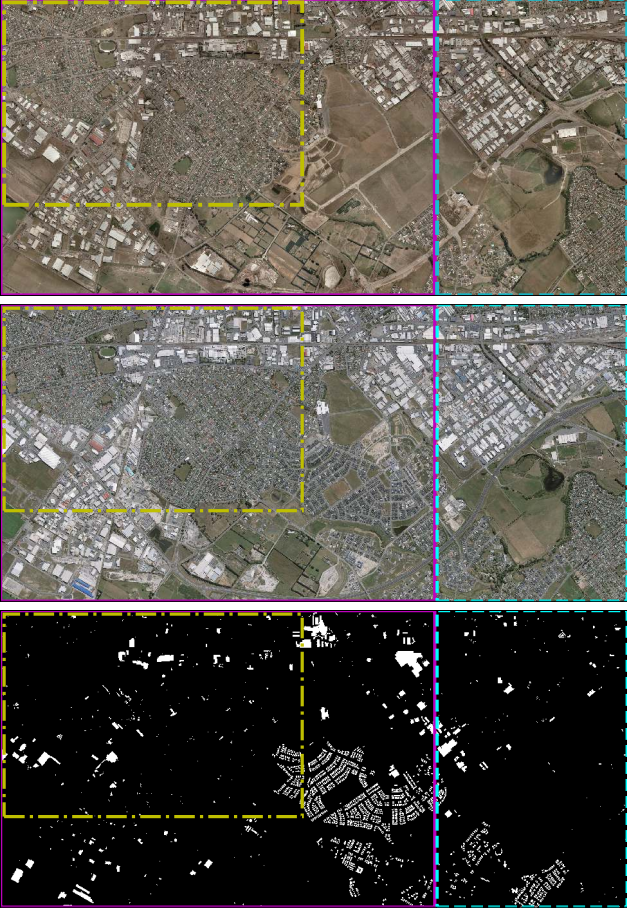


Figure 9: Train - validation - test split of the WHU dataset. The yellow (dash-dot line) rectangle represents the training data. The area between the magenta rectangle (solid line) and the yellow (dash-dot) represents the validation data. Finally, the cyan rectangle (dashed) is the test data. The reasoning for our split is to include in the validation data both industrial and residential areas and isolate (spatially) the training area from the test area in order to avoid spurious spatial correlation between training/test sites.

(Kingma and Ba, 2014). The backbone of each of the networks is described in Table A.3. It can be seen that the convergence and performance of all building blocks equipped with the FracTAL outperform standard Residual units. In particular we find that the performance and convergence properties of the networks follow: ResNet  $\langle$  FracTAL ResNet  $\langle$  CEECNetV1  $\langle$  CEECNetV2. The performance difference between FracTAL ResNet and CEECNetV1 will become more clearly apparent in the change detection datasets. The V2 version of CEECNet that uses Fusion with relative attention (cyan solid line) instead of concatenation (V1 - magenta dashed line), for combining layers in the Compress-Expand and Expand-Compress branches, has superiority over V1. However, it is a computationally more intensive unit.

## 7.2. Evolving loss

In this section, we present experimental results on the performance of the evolving loss strategy using a network with standard ResNet building blocks. The macro topology of the ResNet-based network is identical to the one in Table A.3.

In Fig. 11 we demonstrate the effect of this approach: we train a network on CIFAR10 with standard residual blocks (He et al., 2016, 2015) under two different strategies. In both strategies, we reduce the initial learning rate by a factor of 10 at epochs 250 and 350. In the first strategy, we train the networks with  $\mathcal{FT}^0$ . In the second strategy, we evolve the depth of the fractal Tanimoto loss function: we start training with  $\mathcal{FT}^0$  and on the two subsequent learning rate reductions we use  $\langle \mathcal{FT} \rangle^{15}$  and  $\langle \mathcal{FT} \rangle^{30}$ . In the top panel, we plot the validation accuracy for the two strategies. The performance gain following the evolving depth loss is  $\sim 0.25\%$  in validation accuracy. In the bottom panel we plot the training accuracy. The difference in the training accuracy is  $\sim 2.8\%$ .

We should note that we observed performance degradation by using for training (from random weights) the  $\langle \mathcal{FT} \rangle^d$  for  $d > 1$ . This is evident in Fig. 12 where we train from scratch on CIFAR10 three identical models with different depth for the  $\mathcal{FT}^d$  function:  $d = [0, 3, 6]$ . It is seen that as the hyperparameter  $d$  increases, the performance of the validation accuracy degrades. We consider that this happens due to the low value of the gradients away from optimality, as it requires the network to train longer to reach the same level of validation accuracy. In contrast, the greatest benefit we observed by using this training strategy is that the network can avoid overfitting after learning rate reduction (provided that the slope created by the choice of depth  $d$  is significant) and has the potential to reach higher performance. Interestingly, the degradation of the training loss is not strictly decreasing: the training loss for  $d = 3$  is higher than that for  $d = 0$ . We do not know why this is happening.

## 8. Experimental Design

In this section, we describe the setup of our experiments for the evaluation of the proposed algorithms on the task of change detection. We start by describing the two datasets we used (LEVIRCD Chen and Shi 2020 and WHU Ji et al. 2019b)



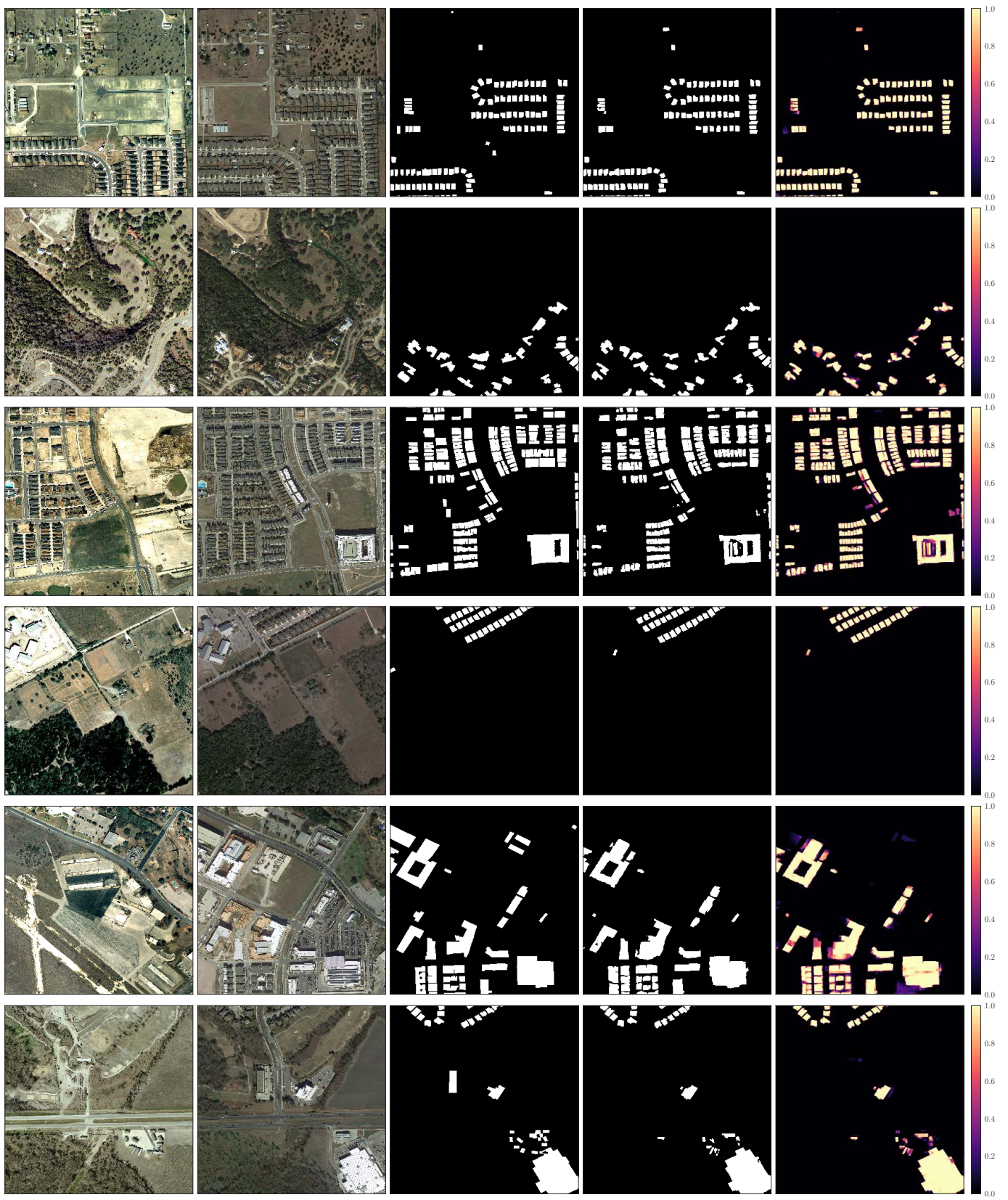


Figure 10: Examples of inferred change detection on some test tiles from the LEVIRCD dataset of the mantis CEECNetV1 model. For each row, from left to right input image date 1, input image date 2, ground truth, change prediction (threshold 0.5) and confidence heat map.



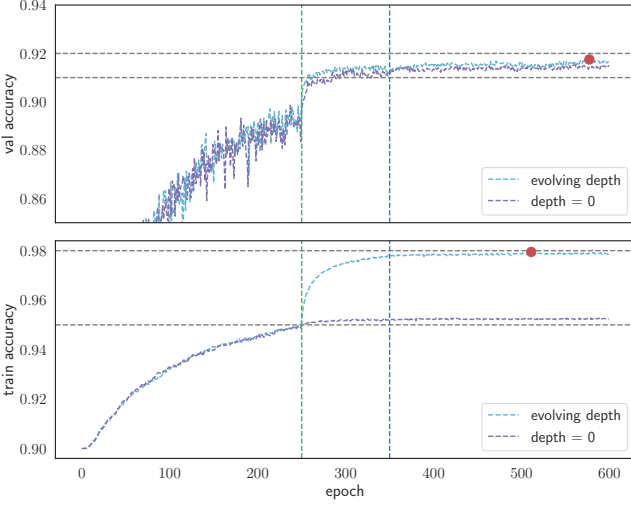


Figure 11: Training on CIFAR10 of a network with standard ResNet building blocks and evolving  $\mathcal{F}\mathcal{T}$  loss strategy. We increase the depth  $d$  of the  $\mathcal{F}\mathcal{T}^d(\mathbf{p}, \mathbf{l})$  loss function with each learning rate reduction. The training accuracy spikes up. The vertical dashed lines designate epochs where the learning rate was scaled to 1/10th of its original value. The validation accuracy is mildly affected, although there is a clear difference. The difference between the training accuracies designates there is a lot of potential in this loss function.

as well as the data augmentation methodology we followed. Then we proceed in describing the metrics used for performance evaluation and the inference methodology. Both mantis CEECNetV1 and mantis FracTAL ResNet have an initial number of filters equal to  $\text{nf}=32$ , and the depth of the encoder branches was equal to 6. We designate these models with D6nf32. In all experiments, we fix the hyper parameter of the FracTAL at  $d = 5$ . We note that we did not evaluate the performance of the mantis CEECNetV2 architecture for the task of change detection, as it is computationally more expensive than V1 that already achieves excellent results<sup>13</sup>.

### 8.1. LEVIRCD Dataset

The LEVIR-CD change detection dataset (Chen and Shi, 2020) consists of 637 pairs of VHR aerial images of resolution 0.5m per pixel. It covers various types of buildings, such as villa residences, small garages, apartments, and warehouses. It contains 31,333 individual building changes. The authors provide a train/validation/test split, which standardizes the performance process. We used a different split for training and validation, however, we used the test set the authors provide for reporting performance. For each tile from the training and validation set, we extracted  $\sim 10\%$  of the area of each tile for extracting validation training chips of size  $256 \times 256$ .

### 8.2. WHU Building Change Detection

The WHU building change dataset (Ji et al., 2019b) consists of two aerial images (2011 and 2016) that cover an area of  $\sim$

<sup>13</sup>The computational complexity of V2 may be owed to a mxnet bug, at the moment of writing this manuscript. In particular, trying to create an optimized CUDA static graph for the mantis CEECNetV2 D6nf32 takes approximately one hour. We are investigating this issue.

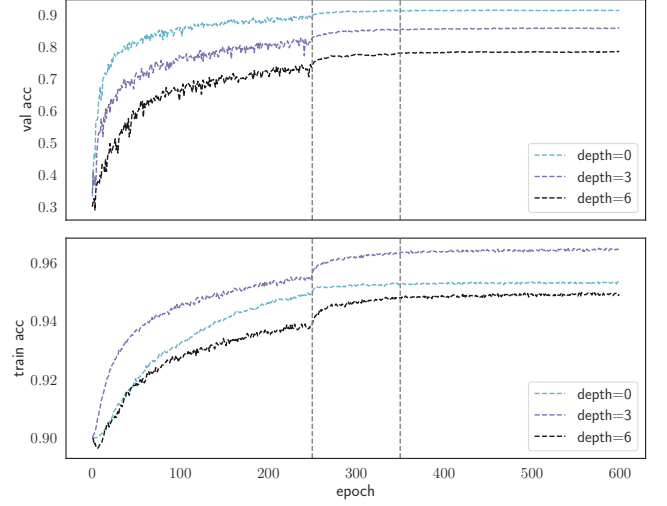


Figure 12: Training on CIFAR10 of a network with standard ResNet building blocks and fixed depth,  $d$ , of the  $\langle \mathcal{F}\mathcal{T}^d \rangle$  loss. The vertical dashed lines designate epochs where the learning rate was scaled to 1/10th of its original value. As the depth of iteration,  $d$ , increases ( $d$  remains constant for each training) the convergence speed of the validation accuracy degrades.

20km<sup>2</sup>, which was changed from 2011 (earthquake) to 2016. The images resolution is 0.3m spatial resolution. The dataset contains 12796 buildings. We split the triplets of images and ground truth change labels, in three areas with ratio 70% for training and validation and 30% for testing. We further split the 70% part in 90% area for training and 10% area for validation. The splitting can be seen in Fig. 9. Note that the training area is spatially separated from the test area (the validation area is in between the two).

### 8.3. Data preprocessing and augmentation

We split the original tiles in training chips of size  $F^2 = 256^2$  by using a sliding window methodology with stride  $s = F/2 = 128$  pixels (the chips are overlapping in half the size of the sliding window). This is the maximum size we can fit to our architecture due to GPU memory limitations that we had at our disposal (NVIDIA P100 16GB). With this batch size we managed to fit a batch size of 3 per GPU for each of the architectures we trained. Due to the small batch size, we used GroupNorm (Wu and He, 2018) for all normalisation layers.

The data augmentation methodology we used during training our network was the one used for semantic segmentation tasks as described in Diakogiannis et al. (2020). That is, random rotations with respect to a random center with a (random) zoom in/out operation. We also implemented random brightness and random polygon shadows. In order to help the algorithm explicitly on the task of the change detection, we implemented time reversal (reversing the order of the input images should not affect the binary change mask) and random identity (we randomly gave as input one of the two images, i.e. null change mask). These latter transformations were implemented at a rate of 50%.

#### 8.4. Metrics

In this section, we present the metrics we used for quantifying the performance of our algorithms. With the exception of the Intersection over Union (IoU) metric, for the evaluation of all other metrics we used the PYTHON library PYCM as described in Haghighi et al. (2018). The statistical measures we used in order to evaluate the performance of our modelling approach are pixel-wise precision, recall, F1 score, Matthews Correlation Coefficient (MCC) (Matthews, 1975) and the Intersection over union. These are defined through:

$$\begin{aligned} \text{precision} &= \frac{TP}{TP + FP} \\ \text{recall} &= \frac{TP}{TP + FN} \\ F1 &= 2 \frac{\text{precision} \times \text{recall}}{\text{precision} + \text{recall}} \\ MCC &= \frac{TP \times TN - FP \times FN}{\sqrt{(TP + FP)(TP + FN)(TN + FP)(TN + FN)}} \\ IoU &= \frac{TP}{TP + FN + FP} \end{aligned}$$

#### 8.5. Inference

In this section, we provide a brief description of the model selection after training (i.e. which epochs will perform best on the test set) as well as the inference methodology we followed for large raster images that exceed the memory capacity of modern-day GPUs.

##### 8.5.1. Inference on large rasters

Our approach is identical to the one used in Diakogiannis et al. (2020), with the difference that now we are processing two input images. Interested readers that want to know the full details can refer to Section 3.4 of Diakogiannis et al. (2020).

During inference on test images, we extract multiple overlapping windows of size  $256 \times 256$  with a step (stride) size of  $256/4 = 64$  pixels. The final prediction “probability”, per pixel, is evaluated as the average “probability” over all inference windows that overlap on the given pixel. In this definition, we refer to “probability” as the output of the softmax final classification layer, which is a continuous value in the range  $[0, 1]$ . It is not a true probability, in the statistical sense, however, it does express the confidence of the algorithm in obtaining the inference result.

With this overlapping approach, we make sure that the pixels that are closer to the edges and correspond to boundary areas for some inference windows, appear closer to the center area of subsequent inference windows. For the boundary pixels of the large raster, we apply reflect padding before performing inference (Ronneberger et al., 2015).

##### 8.5.2. Model selection using Pareto efficiency

For monitoring the performance of our modelling approach, we usually rely on the MCC metric on the validation dataset. We observed, however, that when we perform simultaneously learning rate reduction and  $\langle \mathcal{FT} \rangle^d$  depth increase, initially the

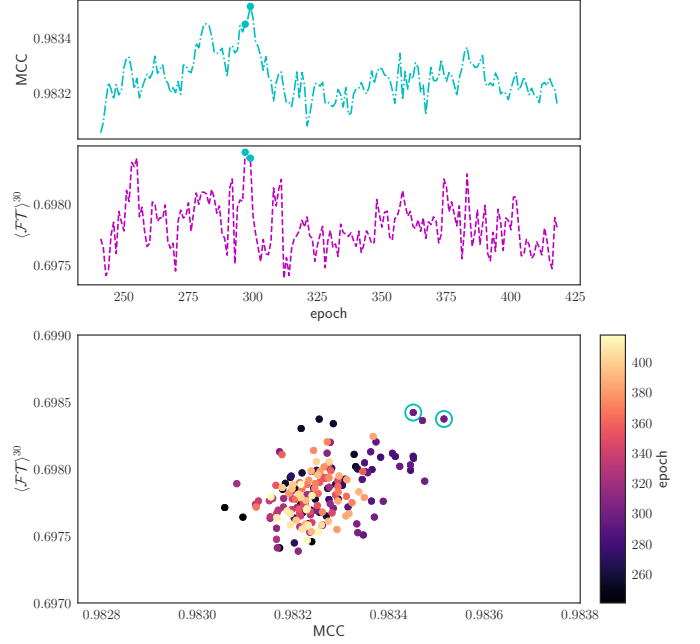


Figure 13: Pareto front selection after the last reduction of learning rate. The bottom panel designates with open cyan circles the two points that are equivalent in terms of quality prediction when both MCC and  $\langle \mathcal{FT} \rangle$  are taken into account. The top two panels show the corresponding evolutions of these measures during training. There, the Pareto optimal points are designated with full circle dots (cyan).

MCC decreases (indicating performance drop), while the  $\langle \mathcal{FT} \rangle^d$  similarity is (initially) strictly increasing. After training starts to stabilize around some optimality region (with the standard noise oscillations), there are various cases where the MCC metric and  $\langle \mathcal{FT} \rangle^d$  similarity coefficient do not agree on which is the best model. To account for this effect and avoid losing good candidate solutions, we evaluate the average of the inference output of a set of best candidate models. These best candidate models are selected according to the models that belong to the Pareto front of the most evolved solutions. We use all the Pareto front (Emmerich and Deutz, 2018) model weights as acceptable solutions for inference. A similar approach was followed for the selection of hyper parameters for optimal solutions in Waldner and Diakogiannis (2020).

In Fig. 13 we plot on the top panel the evolution of the MCC, and  $\langle \mathcal{FT} \rangle^d$  for  $d = 30$ . Clearly, these two performance metrics do not always agree. For example, the  $\langle \mathcal{FT} \rangle^{30}$  is close to optimality in approximate epoch  $\sim 250$ , while the MCC is clearly suboptimal. We highlight with filled circles (cyan dots) the two solutions that belong to the Pareto front. In the bottom panel we plot the correspondence of the MCC values with the  $\langle \mathcal{FT} \rangle^{30}$  similarity metric. The two circles show the corresponding non-dominated Pareto solutions (i.e. best candidates).

## 9. Results

In this section, we report the quantitative and qualitative performance of the models we developed for the task of change

Table 1: Model comparison on the LEVIR building change detection dataset. We designate with **bold** font the best values, and with underline the second best. Both of our frameworks (D6nf32) use the *mantis* macro-topology and achieve state of the art performance.

Model	Precision	Recall	F1	MCC	IoU
Chen and Shi (2020)	83.80	<b>91.00</b>	87.30	-	-
FracTAL ResNet	<u>93.60</u>	89.38	<u>91.44</u>	<u>91.02</u>	<u>84.23</u>
CEECNetV1	<b>93.73</b>	<u>89.93</u>	<b>91.79</b>	<b>91.38</b>	<b>84.82</b>

detection on the LEVIRCD (Chen and Shi, 2020) and WHU (Ji et al., 2019b) datasets.

### 9.1. Performance on LEVIRCD

For this particular dataset, a fixed test set is provided and a comparison with methods that other authors followed is possible. Both FracTAL ResNet and CEECNet outperform the baseline (Chen and Shi, 2020) with respect to the F1 score by  $\sim 5\%$ .

In Fig. 10 we present the inference of the CEECNet algorithm for various images from the test set. For each row, from left to right we have input image at date 1, input image at date 2, ground truth mask, inference (threshold = 0.5), and algorithm’s confidence<sup>14</sup> heat map. It is interesting to note that the algorithm has zero doubt in areas where buildings exist in both input images. That is, it is clear our algorithm identifies change in areas covered by buildings, and not building footprints. In Table 1 we present numerical performance results of both FracTAL ResUNet as well as CEECNet. All metrics, precision, recall, F1, MCC and IoU are excellent. The *mantis* CEECNet outperforms the *mantis*FracTAL ResNet by a small numerical margin, however the difference is clear. This difference can also be seen in the bottom panel of Fig. 15. We should also note that the numerical difference on, say, F1 score, does not translate to equal portions of quality difference in images. That is, a 1% difference in F1 score, may have a significant impact on the quality of inference. We further discuss this on Section 9.4.

### 9.2. Performance on WHU

In Table 2 we present the results of training FracTAL ResNet and CEECNet building blocks. Both of our proposed architectures outperforms all other modeling frameworks, although we need to stress that each of the other authors followed a different splitting strategy of the data. In particular, Ji et al. (2019a) used half of the raster for training and validation, and the other half for testing. There should be some performance increase in their model if they followed our splitting strategy (we used only 30% of the total area for testing) however this is not something we can quantify. On the other hand, there is no spatial separation between training and test sites, as it exists in our case, and this should work in their advantage. Also, the usage of a larger window for training (their extracted chips are of spatial dimension  $512 \times 512$ ) increases in principle the performance because

Table 2: Model comparison on the WHU building change detection dataset. We denote with **bold** the top ranking solutions, and with underline the second best. We designate with **bold** font the best values, and with underline the second best. Ji et al. (2019a) presented two models for extracting buildings prior estimating the change mask. These were the Mask-RCNN (in table: M1) and MS-FCN (in table: M2). Our models consume input images of size of  $256 \times 256$  pixels. With the exception of Liu et al. (2019) that uses the same size, all other results consume inputs of size of  $512 \times 512$  pixels.

Model	Precision	Recall	F1	MCC	IoU
Ji et al. (2019a) M1	93.100	89.200	91.108	-	83.70
Ji et al. (2019a) M2	93.800	87.800	90.700	-	83.00
Chen et al. (2020)	89.2	90.5	89.80	-	-
Cao et al. (2020)	94.00	79.37	86.07	-	-
Liu et al. (2019)	90.15	89.35	89.75	-	81.40
FracTAL ResNet	<u>95.350</u>	<u>90.873</u>	<u>93.058</u>	<u>92.892</u>	<u>87.02</u>
CEECNetV1	<b>95.571</b>	<b>92.043</b>	<b>93.774</b>	<b>93.616</b>	<b>88.23</b>

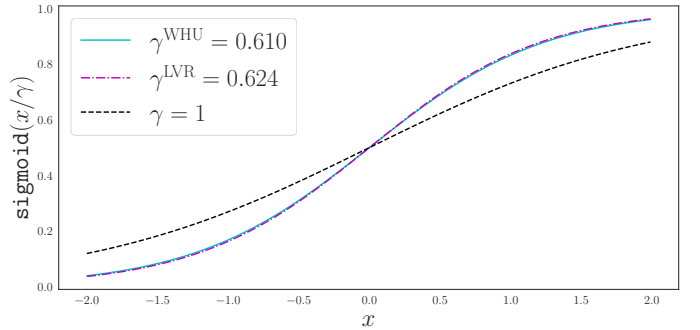


Figure 14: Trainable scaling parameters,  $\gamma$ , for the sigmoid activation, i.e.  $\text{sigmoid}(x/\gamma)$ , that are used in the prediction of change mask boundary layers.

it includes more context information. There is a tradeoff here though, in that using a larger window size reduces the number of available training chips. Chen et al. (2020) split randomly their training and validation chips. This should improve performance, because there is a tight spatial correlation for two extracted chips that are in geospatial proximity. Cao et al. (2020) used as a test set  $\sim 20\%$  of the total area of the WHU dataset for training, however, they do not specify the splitting strategy they followed. Finally, Liu et al. (2019) used approximately  $\sim 10\%$  of the total area for reporting test score performance. They also do not mention their splitting strategy.

In this table we could not include (Jiang et al., 2020, PGA-SiamNet) that report performance results evaluated only on the changed pixels, and not the complete test images. Thus, they are missing out all false positive predictions that can have a dire impact on the performance metrics. They report precision: 97.840, recall: 97.01, F1: 97.29 and IoU: 97.38.

In Fig. B.19 we plot from left to right, the test area on date 1, the test area on date 2, the ground truth mask, and the confidence heat map of these predictions. In Fig. 16 we plot a set of examples of inference on the WHU dataset. The correspondence of the images in each row is identical to Fig. 10, with the addition that we denote with blue rectangles the locations of changed buildings (true positive predictions), and with red

<sup>14</sup>This should not be confused with statistical confidence.

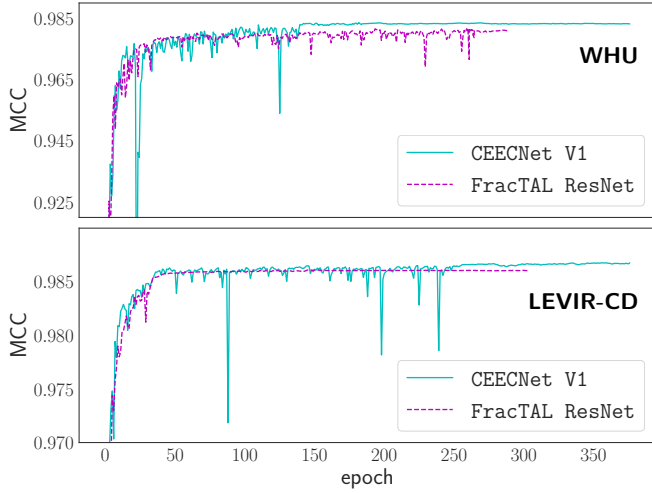


Figure 15: mantis CEECNetV1 vs mantis FracTAL ResNet evolution performance on change detection validation datasets. The top panel corresponds to the LEVIRCD dataset. The bottom panel to the WHU dataset. For each networks we followed the evolving loss strategy: there are two learning rate reductions followed by two scaling ups of the  $\langle \mathcal{FT} \rangle^d$  loss function. All four training histories avoid overfitting, thanks to making the loss function sharper towards optimality.

squares missed changes from our model (false negative). It can be seen that the most difficult areas are the ones that are heavily populated/heavily built up, and the changes are small area buildings.

### 9.3. The effect of scaled sigmoid on the segmentation HEAD

Starting from an initial value  $\gamma = 1$  of the scaled sigmoid boundary layer, the fully trained model mantis CEECNetV1 learns the following parameters that control how “crisp” the boundaries should be, or else, how sharp the decision boundary should be:

$$\begin{aligned}\gamma_{\text{sigmoid}}^{\text{LVR}} &= 0.610 \\ \gamma_{\text{sigmoid}}^{\text{WHU}} &= 0.625\end{aligned}$$

The deviation of these coefficients from their initial values, demonstrates that indeed the network finds useful to modify the decision boundary. In Fig. 14 we plot the standard sigmoid function ( $\gamma = 1$ ) and the sigmoid functions recovered after training on the LEVIRCD and WHU datasets.

The algorithm in both cases learns to modify the decision boundary, by making it sharper. This means that for two nearby pixels, one belonging to a boundary, the other to a background class, the numerical distance between them needs to be smaller to achieve class separation, in comparison with standard sigmoid. Or else, a small  $\delta x$  change is sufficient to transition between boundary and no-boundary class.

### 9.4. Qualitative CEECNet and FracTAL performance

Although both CEECNet and FracTAL ResNet achieve a very high MCC (Fig. 15), the superiority of CEECNet is evident in the inference maps in both the LEVIRCD (Fig. 17) and

WHU (Fig. 18) datasets. This confirms their relative scores (Tables 1 and 2) and the faster convergence of CEECNet (Fig 8). Interestingly, CEECNet predicts change with more confidence than FracTAL ResNet (Figures 17 and 18), even when it errs, as can be seen from the corresponding confidence heat maps.

The decision on which of the two models one should use is a decision to be made with respect to the relative “cost” of training each model and available hardware resources.

## 10. Conclusions

In this work, we propose a new deep learning framework for the task of semantic change detection on very high resolution aerial images, presented here for the case of changes in buildings. This framework is built on top of several novel contributions that can be used independently in computer vision tasks. Our contributions are:

1. A novel set similarity coefficient, the fractal Tanimoto coefficient, that is derived from a variant of the Dice coefficient. This coefficient can provide finer detail of similarity, at a desired level (up to a delta function), and this is regulated by a temperature-like hyper-parameter,  $d$  (Fig. 2).
2. A novel training loss scheme, where we use an evolving loss function, that changes according to learning rate reductions. This helps avoid overfitting and allows for a small increase in performance (Figures 11 & 12). In particular, this scheme provided 0.25% performance increase in validation accuracy, and 2.8% increase in the training accuracy. Although we are mostly interested in the validation accuracy, the training accuracy difference suggests that perhaps there is more potential in this training scheme that we did not manage to unlock.
3. A novel spatial and channel attention layer, the fractal Tanimoto Attention Layer (FracTAL - see Listing 2), that uses the fractal Tanimoto similarity coefficient as a means of quantifying the similarity between query and key entries. This layer is memory efficient and scales well with the size of input features.
4. A novel building block, the FracTAL ResNet (Fig 4), that has a small memory footprint and excellent convergent and performance properties that outperform standard ResNet building blocks.
5. A novel building block, the Compress/Expand - Expand/Compress (CEECNet) unit (Fig. 5), that has better performance than the FracTAL ResNet (Fig. 15), that comes, however, at a higher computational cost.
6. A corollary that follows from the introduced building blocks, is a novel fusion methodology of layers and their corresponding attentions, both for self and relative attention, that improves performance (Fig. 15). This methodology can be used as a direct replacement of concatenation in convolution neural networks.
7. A novel macro-topology (backbone) architecture, the mantis topology (Fig. 6), that combines the building blocks we



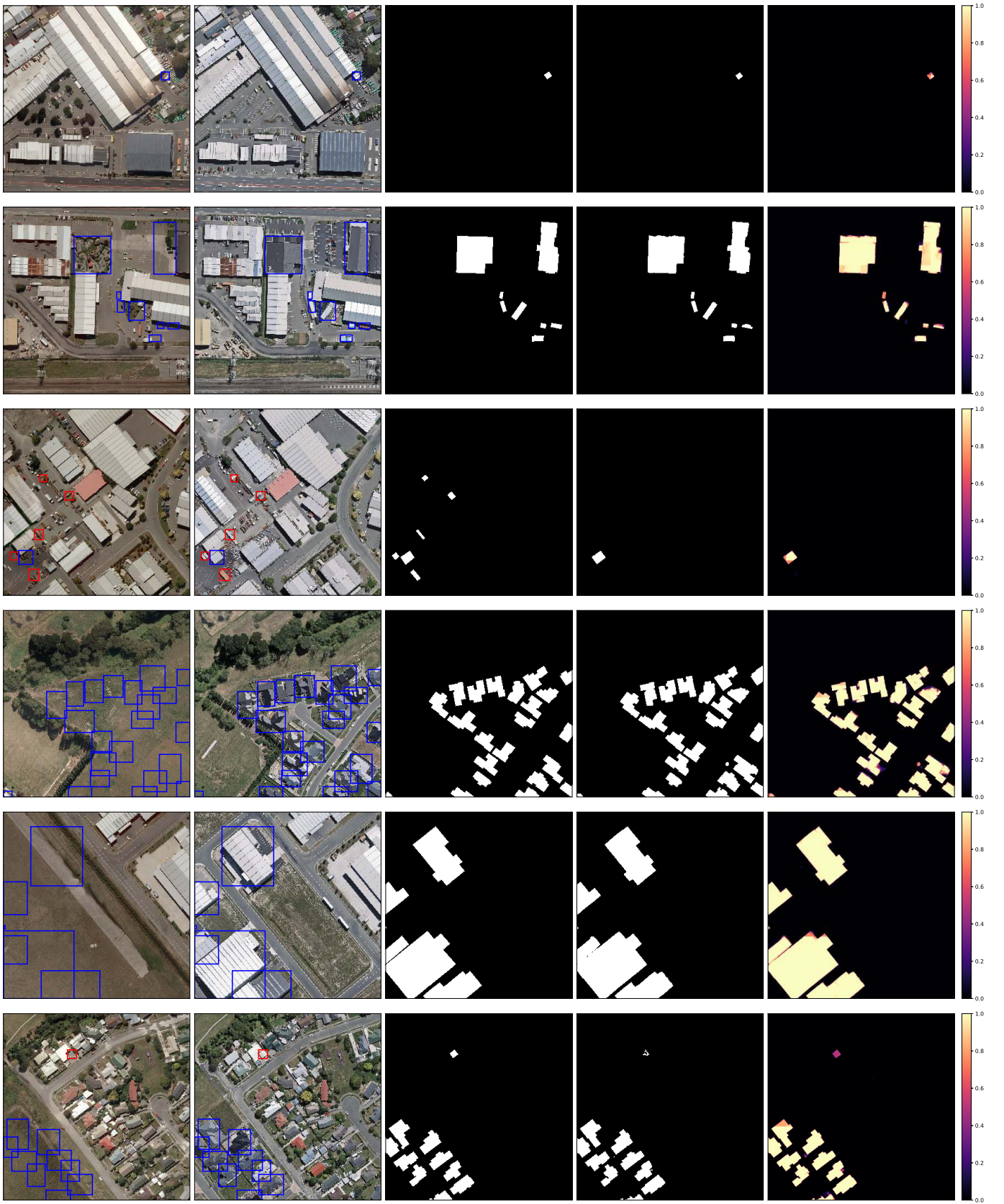


Figure 16: Sample of change detection on windows of size  $1024 \times 1024$  from the WHU NZ dataset. Inference is with the `mantis CEECNetV1` model. The ordering of the inputs, for each row, is as in Fig. 10. We indicate with blue boxes successful findings and with red boxes missed changes on buildings.



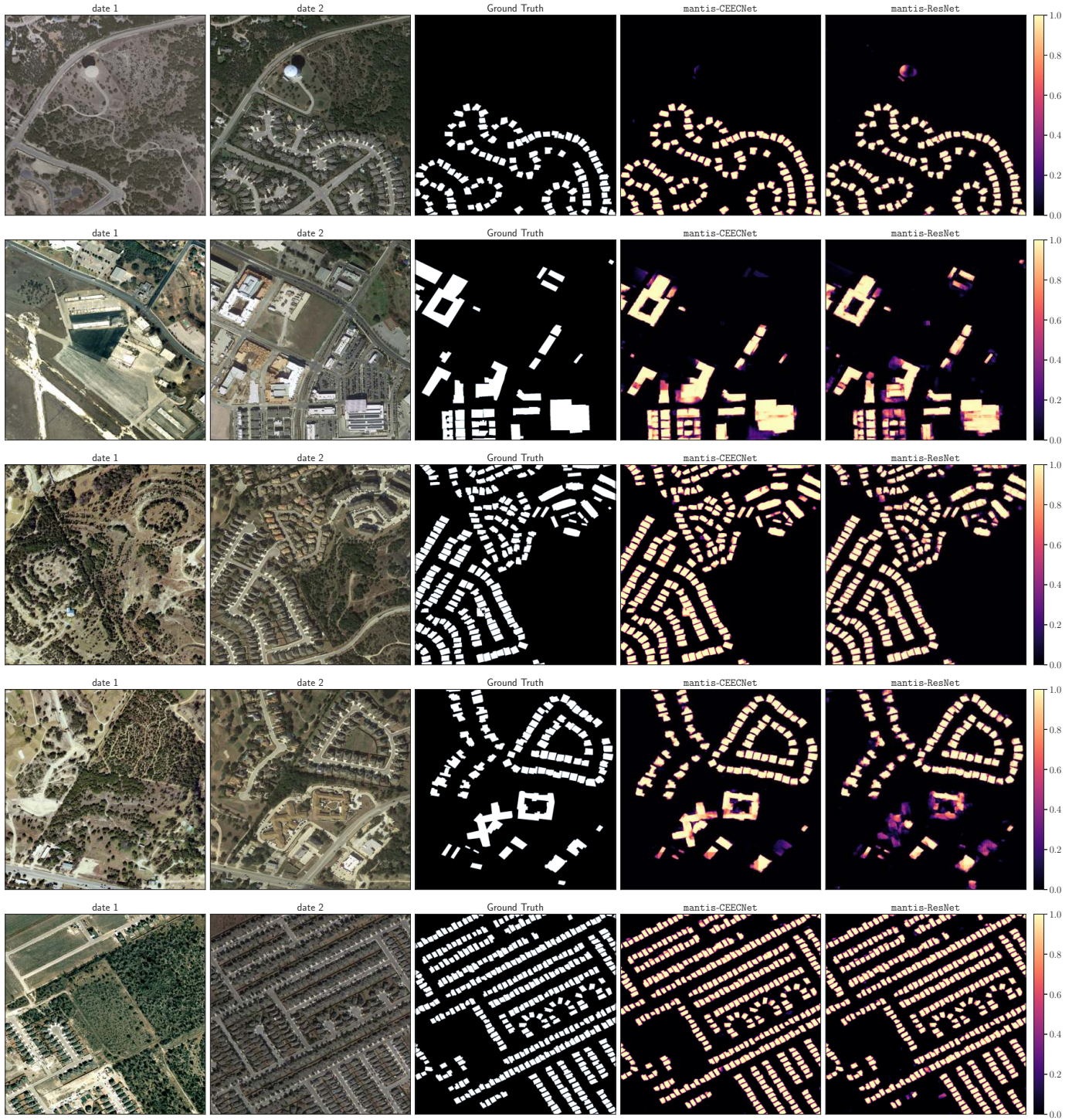


Figure 17: Samples of relative quality change detection on test tiles of size  $1024 \times 1024$  from the LEVIRCD dataset. For each row from left to right: input image date 1, input image date 2, ground truth, confidence heat maps of mantis CEECNetV1 and mantis FracTAL ResNet respectively.



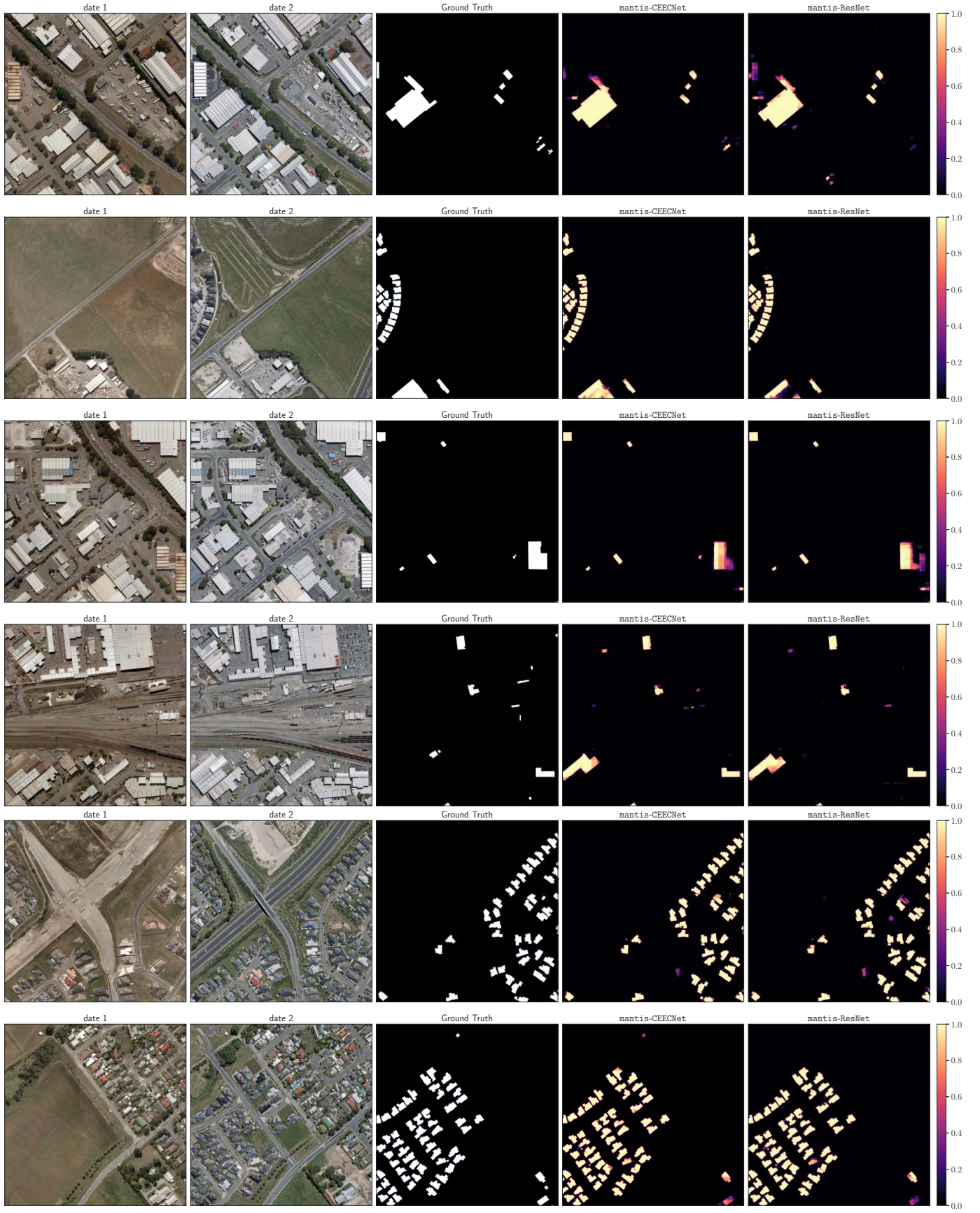


Figure 18: As in Fig. 17 for sample windows of size  $2048 \times 2048$  from the WHU NZ dataset.

developed and is able to consume images from two different dates and produce a single change detection layer. It should be noted that the same topology can be used in general segmentation problems, where we have two input images to a network that are somehow correlated and produce a semantic map.

Putting all things together, both of the proposed networks that presented in this contribution, mantis FracTAL ResNet and mantis CEECNetV1, outperform other proposed networks and achieve state of the art results on the LEVIRCD (Chen and Shi, 2020) and the WHU<sup>15</sup> (Ji et al., 2019b) building change detection datasets (Tables 1 & 2). In comparison with state of the art architectures that use atrous dilated convolutions, the proposed architectures do not require fine tuning of the dilation rates. Therefore, they are simpler, and easier to set up and train.

In this work we did not experiment with deeper architectures, that would surely improve performance (e.g. D7nf32 models usually perform better), or with hyper parameter tuning. We also did not test the mantis CEECNetV2 model on the task of change detection, because it was computationally too expensive (this may be owed to a MXNET bug, at the moment of writing this manuscript).

## Acknowledgments

This project was supported by resources and expertise provided by CSIRO IMT Scientific Computing. The authors acknowledge the support of the MXNET community.

## References

### References

Alcantarilla, P.F., Stent, S., Ros, G., Arroyo, R., Gherardi, R., 2016. Street-view change detection with deconvolutional networks, in: *Proceedings of Robotics: Science and Systems*, Ann Arbor, Michigan. doi:10.15607/RSS.2016.XII.044.

Asokan, A., Anitha, J., 2019. Change detection techniques for remote sensing applications: a survey. *Earth Science Informatics* 12, 143–160. URL: <https://doi.org/10.1007/s12145-019-00380-5>, doi:10.1007/s12145-019-00380-5.

Bahdanau, D., Cho, K., Bengio, Y., 2014. Neural machine translation by jointly learning to align and translate. URL: <http://arxiv.org/abs/1409.0473>, cite arxiv:1409.0473Comment: Accepted at ICLR 2015 as oral presentation.

Bello, I., Zoph, B., Vaswani, A., Shlens, J., Le, Q.V., 2019. Attention augmented convolutional networks. *CoRR abs/1904.09925*. URL: <http://arxiv.org/abs/1904.09925>, arXiv:1904.09925.

Cao, Z., Wu, M., Yan, R., Zhang, F., Wan, X., 2020. Detection of small changed regions in remote sensing imagery using convolutional neural network. *IOP Conference Series: Earth and Environmental Science* 502, 012017. URL: <https://doi.org/10.1088/1755-1315/502/1/012017>, doi:10.1088/1755-1315/502/1/012017.

Cayé Daudt, R., Le Saux, B., Boulch, A., Gousseau, Y., 2019. Multitask learning for large-scale semantic change detection. *Computer Vision and Image Understanding* 187, 102783. URL: <http://www.sciencedirect.com/science/article/pii/S1077314219300992>, doi:https://doi.org/10.1016/j.cviu.2019.07.003.

<sup>15</sup>Note that there is not standardized test set for the WHU dataset, therefore relative performance is indicative but not absolute: it depends on the train/test split that other researchers have performed.

Chen, H., Shi, Z., 2020. A spatial-temporal attention-based method and a new dataset for remote sensing image change detection. *Remote Sensing* 12. URL: <https://www.mdpi.com/2072-4292/12/10/1662>, doi:10.3390/rs12101662.

Chen, J., Yuan, Z., Peng, J., Chen, L., Huang, H., Zhu, J., Lin, T., Li, H., 2020. Dasnet: Dual attentive fully convolutional siamese networks for change detection of high resolution satellite images. *arXiv:2003.03608*.

Chen, L., Zhang, H., Xiao, J., Nie, L., Shao, J., Chua, T., 2016. SCA-CNN: spatial and channel-wise attention in convolutional networks for image captioning. *CoRR abs/1611.05594*. URL: <http://arxiv.org/abs/1611.05594>, arXiv:1611.05594.

Chen, T., Li, M., Li, Y., Lin, M., Wang, N., Wang, M., Xiao, T., Xu, B., Zhang, C., Zhang, Z., 2015. Mxnet: A flexible and efficient machine learning library for heterogeneous distributed systems. *arXiv preprint arXiv:1512.01274*.

Cho, K., van Merriënboer, B., Bahdanau, D., Bengio, Y., 2014. On the properties of neural machine translation: Encoder-decoder approaches. *CoRR abs/1409.1259*. URL: <http://arxiv.org/abs/1409.1259>, arXiv:1409.1259.

Coppin, P., Jonckheere, I., Nackaerts, K., Muys, B., Lambin, E., 2004. Review article digital change detection methods in ecosystem monitoring: a review. *International journal of remote sensing* 25, 1565–1596.

Daudt, R.C., Le Saux, B., Boulch, A., Gousseau, Y., 2019. Multitask learning for large-scale semantic change detection. *Computer Vision and Image Understanding* 187, 102783.

Diakogiannis, F.I., Waldner, F., Caccetta, P., Wu, C., 2020. Resunet-a: A deep learning framework for semantic segmentation of remotely sensed data. *ISPRS Journal of Photogrammetry and Remote Sensing* 162, 94 – 114. URL: <http://www.sciencedirect.com/science/article/pii/S0924271620300149>, doi:https://doi.org/10.1016/j.isprsjprs.2020.01.013.

Emmerich, M.T., Deutz, A.H., 2018. A tutorial on multiobjective optimization: Fundamentals and evolutionary methods. *Natural Computing: An International Journal* 17, 585609. URL: <https://doi.org/10.1007/s11047-018-9685-y>, doi:10.1007/s11047-018-9685-y.

Giustarini, L., Hostache, R., Matgen, P., Schumann, G.J.P., Bates, P.D., Mason, D.C., 2012. A change detection approach to flood mapping in urban areas using terrasar-x. *IEEE transactions on Geoscience and Remote Sensing* 51, 2417–2430.

Guo, E., Fu, X., Zhu, J., Deng, M., Liu, Y., Zhu, Q., Li, H., 2018. Learning to measure change: Fully convolutional siamese metric networks for scene change detection. *CoRR abs/1810.09111*. URL: <http://arxiv.org/abs/1810.09111>, arXiv:1810.09111.

Haghighi, S., Jasemi, M., Hessabi, S., Zolanvari, A., 2018. PyCM: Multiclass confusion matrix library in python. *Journal of Open Source Software* 3, 729. URL: <https://doi.org/10.21105/joss.00729>, doi:10.21105/joss.00729.

He, K., Gkioxari, G., Dollár, P., Girshick, R.B., 2017. Mask R-CNN. *CoRR abs/1703.06870*. URL: <http://arxiv.org/abs/1703.06870>, arXiv:1703.06870.

He, K., Zhang, X., Ren, S., Sun, J., 2015. Deep residual learning for image recognition. *CoRR abs/1512.03385*. URL: <http://arxiv.org/abs/1512.03385>, arXiv:1512.03385.

He, K., Zhang, X., Ren, S., Sun, J., 2016. Identity mappings in deep residual networks. *CoRR abs/1603.05027*. URL: <http://arxiv.org/abs/1603.05027>, arXiv:1603.05027.

Hu, J., Shen, L., Sun, G., 2017. Squeeze-and-excitation networks. *CoRR abs/1709.01507*. URL: <http://arxiv.org/abs/1709.01507>, arXiv:1709.01507.

Hussain, M., Chen, D., Cheng, A., Wei, H., Stanley, D., 2013a. Change detection from remotely sensed images: From pixel-based to object-based approaches. *ISPRS Journal of photogrammetry and remote sensing* 80, 91–106.

Hussain, M., Chen, D., Cheng, A., Wei, H., Stanley, D., 2013b. Change detection from remotely sensed images: From pixel-based to object-based approaches. *ISPRS Journal of Photogrammetry and Remote Sensing* 80, 91 – 106. URL: <http://www.sciencedirect.com/science/article/pii/S0924271613000804>, doi:https://doi.org/10.1016/j.isprsjprs.2013.03.006.

Ioffe, S., Szegedy, C., 2015. Batch normalization: Accelerating deep network training by reducing internal covariate shift. *CoRR abs/1502.03167*. URL: <http://arxiv.org/abs/1502.03167>, arXiv:1502.03167.



- Ji, S., Shen, Y., Lu, M., Zhang, Y., 2019a. Building instance change detection from large-scale aerial images using convolutional neural networks and simulated samples. *Remote Sensing* 11. URL: <https://www.mdpi.com/2072-4292/11/11/1343>, doi:10.3390/rs11111343.
- Ji, S., Wei, S., Lu, M., 2019b. Fully convolutional networks for multisource building extraction from an open aerial and satellite imagery data set. *IEEE Transactions on Geoscience and Remote Sensing* 57, 574–586.
- Jiang, H., Hu, X., Li, K., Zhang, J., Gong, J., Zhang, M., 2020. Pga-siamnet: Pyramid feature-based attention-guided siamese network for remote sensing orthoimagery building change detection. *Remote Sensing* 12. URL: <https://www.mdpi.com/2072-4292/12/3/484>, doi:10.3390/rs12030484.
- Kim, Y., Denton, C., Hoang, L., Rush, A.M., 2017. Structured attention networks. *CoRR* abs/1702.00887. URL: <http://arxiv.org/abs/1702.00887>, arXiv:1702.00887.
- Kingma, D.P., Ba, J., 2014. Adam: A method for stochastic optimization. *CoRR* abs/1412.6980. URL: <http://arxiv.org/abs/1412.6980>, arXiv:1412.6980.
- Kingma, D.P., Welling, M., 2019. An introduction to variational autoencoders. *CoRR* abs/1906.02691. URL: <http://arxiv.org/abs/1906.02691>, arXiv:1906.02691.
- Krizhevsky, A., 2009. Learning multiple layers of features from tiny images. Technical Report.
- Lindeberg, T., 1994. *Scale-Space Theory in Computer Vision*. Kluwer Academic Publishers, USA.
- Liu, J., Wang, S., Hou, X., Song, W., 2020. A deep residual learning serial segmentation network for extracting buildings from remote sensing imagery. *International Journal of Remote Sensing* 41, 5573–5587. URL: <https://doi.org/10.1080/01431161.2020.1734251>, doi:10.1080/01431161.2020.1734251, arXiv:https://doi.org/10.1080/01431161.2020.1734251.
- Liu, Y., Pang, C., Zhan, Z., Zhang, X., Yang, X., 2019. Building change detection for remote sensing images using a dual task constrained deep siamese convolutional network model. arXiv:1909.07726.
- Löw, F., Prishchepov, A.V., Waldner, F., Dubovyk, O., Akramkhanov, A., Biradar, C., Lamers, J., 2018. Mapping cropland abandonment in the aral sea basin with modis time series. *Remote Sensing* 10, 159.
- Lu, D., Mausel, P., Brondizio, E., Moran, E., 2004. Change detection techniques. *International journal of remote sensing* 25, 2365–2401.
- Lu, X., Wang, W., Ma, C., Shen, J., Shao, L., Porikli, F., 2019. See more, know more: Unsupervised video object segmentation with co-attention siamese networks, in: *The IEEE Conference on Computer Vision and Pattern Recognition (CVPR)*.
- Matthews, B., 1975. Comparison of the predicted and observed secondary structure of t4 phage lysozyme. *Biochimica et Biophysica Acta (BBA) - Protein Structure* 405, 442 – 451. URL: <http://www.sciencedirect.com/science/article/pii/0005279575901099>, doi:https://doi.org/10.1016/0005-2795(75)90109-9.
- Morton, D.C., DeFries, R.S., Shimabukuro, Y.E., Anderson, L.O., Del Bon Espirito-Santo, F., Hansen, M., Carroll, M., 2005. Rapid assessment of annual deforestation in the brazilian amazon using modis data. *Earth Interactions* 9, 1–22.
- Newell, A., Yang, K., Deng, J., 2016. Stacked hourglass networks for human pose estimation. *CoRR* abs/1603.06937. URL: <http://arxiv.org/abs/1603.06937>, arXiv:1603.06937.
- Oliphant, T.E., 2006. *A guide to NumPy*. volume 1. Trelgol Publishing USA.
- Qin, X., Zhang, Z., Huang, C., Dehghan, M., Zaiane, O.R., Jagersand, M., 2020. U2-net: Going deeper with nested u-structure for salient object detection. *Pattern Recognition* 106, 107404. URL: <http://dx.doi.org/10.1016/j.patcog.2020.107404>, doi:10.1016/j.patcog.2020.107404.
- Ronneberger, O., Fischer, P., Brox, T., 2015. U-net: Convolutional networks for biomedical image segmentation. *CoRR* abs/1505.04597. URL: <http://arxiv.org/abs/1505.04597>, arXiv:1505.04597.
- Sakurada, K., Okatani, T., 2015. Change detection from a street image pair using cnn features and superpixel segmentation, in: *BMVC*.
- Sergeev, A., Balso, M.D., 2018. Horovod: fast and easy distributed deep learning in TensorFlow. arXiv preprint arXiv:1802.05799.
- Shi, W., Zhang, M., Zhang, R., Chen, S., Zhan, Z., 2020. Change detection based on artificial intelligence: State-of-the-art and challenges. *Remote Sensing* 12, 1688. URL: <http://dx.doi.org/10.3390/rs12101688>, doi:10.3390/rs12101688.
- Tewkesbury, A.P., Comber, A.J., Tate, N.J., Lamb, A., Fisher, P.F., 2015. A critical synthesis of remotely sensed optical image change detection techniques. *Remote Sensing of Environment* 160, 1–14.
- Treisman, A.M., Gelade, G., 1980. A feature-integration theory of attention. *Cognitive Psychology* 12, 97 – 136. URL: <http://www.sciencedirect.com/science/article/pii/0010028580900055>, doi:https://doi.org/10.1016/0010-0285(80)90005-5.
- Tschannen, M., Bachem, O., Lucic, M., 2018. Recent advances in autoencoder-based representation learning. *CoRR* abs/1812.05069. URL: <http://arxiv.org/abs/1812.05069>, arXiv:1812.05069.
- Varghese, A., Gubbi, J., Ramaswamy, A., Balamuralidhar, P., 2018. Changenet: A deep learning architecture for visual change detection, in: *Proceedings of the European Conference on Computer Vision (ECCV) Workshops*.
- Vaswani, A., Shazeer, N., Parmar, N., Uszkoreit, J., Jones, L., Gomez, A.N., Kaiser, L., Polosukhin, I., 2017. Attention is all you need. *CoRR* abs/1706.03762. URL: <http://arxiv.org/abs/1706.03762>, arXiv:1706.03762.
- Waldner, F., Diakogiannis, F.I., 2020. Deep learning on edge: Extracting field boundaries from satellite images with a convolutional neural network. *Remote Sensing of Environment* 245, 111741. URL: <http://www.sciencedirect.com/science/article/pii/S0034425720301115>, doi:https://doi.org/10.1016/j.rse.2020.111741.
- Wang, X., Girshick, R.B., Gupta, A., He, K., 2017. Non-local neural networks. *CoRR* abs/1711.07971. URL: <http://arxiv.org/abs/1711.07971>, arXiv:1711.07971.
- Wang, Z., Chen, J., Hoi, S.C.H., 2019. Deep learning for image super-resolution: A survey. *CoRR* abs/1902.06068. URL: <http://arxiv.org/abs/1902.06068>, arXiv:1902.06068.
- Wu, Y., He, K., 2018. Group normalization. *CoRR* abs/1803.08494. URL: <http://arxiv.org/abs/1803.08494>, arXiv:1803.08494.
- Zhang, A., Lipton, Z.C., Li, M., Smola, A.J., 2020. Dive into Deep Learning. <https://d2l.ai>.
- Zhang, H., Goodfellow, I., Metaxas, D., Odena, A., 2018. Self-attention generative adversarial networks. arXiv:1805.08318.
- Zhao, H., Shi, J., Qi, X., Wang, X., Jia, J., 2017. Pyramid scene parsing network, in: *CVPR*.

## Appendix A. CIFAR10 comparison network characteristics

In Table A.3 we present in detail the characteristics of the layers that we used to compare on the CIFAR10 dataset. All building blocks use kernel size = 3 and padding = 1 (SAME).

## Appendix B. Inference across WHU test set

The inference for the best performing model, the mantis CEECNetV1 D6nf32 model can be seen on Fig. B.19. The predictions match very closely the ground truth.

## Appendix C. Algorithms

Here we present with MXNET style pseudocode the implementation of the FracTAL associated modules. In all the listings presented, Conv2DN is a sequential combination of a 2D convolution followed by a normalization layer. When the batch size is very small, due to GPU memory normalization (e.g. smaller than 4 datums per GPU), the normalization used was Group Normalization Wu and He (2018). Practically, in all mantis CEECNet realizations for change detection, we used GroupNorm.

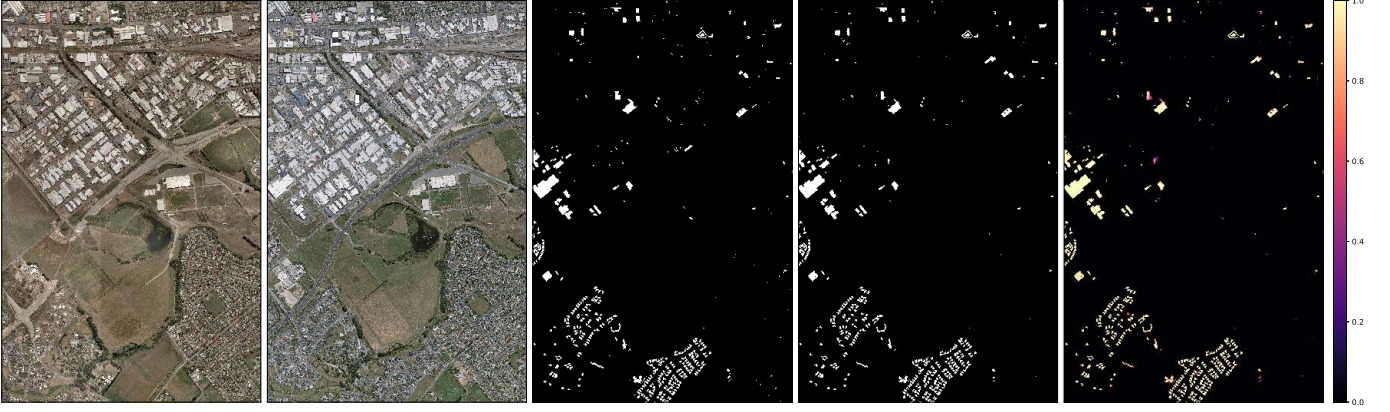


Figure B.19: Inference across the whole test area over NZBLDG CD Dataset using the mantisCEEKNetV1 D6nf32 model. From left to right: 2011 input image, 2016 input image, ground truth, prediction (threshold 0.5) and confidence heat map.

Table A.3: CEEKNetV1 vs CEEKNetV2 vs FracTAL ResNet vs ResNet building blocks comparison. All Building Blocks use kernel size  $k=3$  and padding  $p=1$  (SAME) and stride  $s=1$ . The transition convolutions that half the size of the features use the same kernel size and padding, however the stride is  $s=2$ . In the following we indicate with  $nf$  the number of output channels of the convolution layers, and with  $nh$  the number of heads in the multihead FracTAL module.

Layers	Proposed Models	ResNet
Layer 1	BBlock[nf=64,nh=8]	BBlock[nf=64]
Layer 2	BBlock[nf=64,nh=8]	BBlock[nf=64]
Layer 3	Conv2DN(nf=128,s=2)	Conv2DN(nf=128,s=2)
Layer 4	BBlock[nf=128,nh=16]	BBlock[nf=128]
Layer 5	BBlock[nf=128,nh=16]	BBlock[nf=128]
Layer 6	Conv2DN(nf=256,s=2)	Conv2DN(nf=256,s=2)
Layer 7	BBlock[nf=256,nh=32]	BBlock[nf=256]
Layer 8	BBlock[nf=256,nh=32]	BBlock[nf=256]
Layer 9	ReLU	ReLU
Layer 10	DenseN(nf=4096)	DenseN(nf=4096)
Layer 11	ReLU	ReLU
Layer 12	DenseN(nf=512)	DenseN(nf=512)
Layer 13	ReLU	ReLU
Layer 14	DenseN(nf=10)	DenseN(nf=10)

### Appendix C.1. Fractal Tanimoto Attention 2D module

Listing 1: MXNET/GLUON style pseudo code for the fractal Tanimoto coefficient, predefined for spatial similarity.

```

from mxnet.gluon import nn
class FTanimoto(nn.Block):
    def __init__(self, depth=5, axis=[2,3], **kwargs):
        super().__init__(**kwargs)
        self.depth = depth
        self.axis=axis

    def inner_prod(self, prob, label):
        prdct = prob*label #dim:(B,C,H,W)
        prdct = prdct.sum(axis=self.axis, keepdims=True)
        return prdct #dim:(B,C,1,1)

    def forward(self, prob, label):
        a = 2.**self.depth
        b = -(2.*a-1.)

        tpl= self.inner_prod(prob, label)
        tpp= self.inner_prod(prob, prob)
        tll= self.inner_prod(label, label)

        denum = a*(tpp+tll)+b*tpl
        ftnmt = tpl/denum
        return ftnmt #dim:(B,C,1,1)

```

Listing 2: MXNET/GLUON style pseudocode for the fractal Tanimoto Attention module

```

from mxnet import nd as F
from mxnet.gluon import nn
class FTAttention2D(nn.Block):
    def __init__(self, nchannels, nheads, **kwargs):
        super().__init__(**kwargs)

```

```

self.q = Conv2DN(nchannels, groups=nheads)
self.k = Conv2DN(nchannels, groups=nheads)
self.v = Conv2DN(nchannels, groups=nheads)
# spatial/channel similarity
self.SpatialSim = FTanimoto(axis=[2,3])
self.ChannelSim = FTanimoto(axis=1)
self.norm = nn.BatchNorm()

def forward(self, qin, kin, vin):
    # query, key, value
    q = F.sigmoid(self.q(qin)) #dim:(B,C,H,W)
    k = F.sigmoid(self.k(vin)) #dim:(B,C,H,W)
    v = F.sigmoid(self.v(kin)) #dim:(B,C,H,W)

    att_spat = self.ChannelSim(q,k) #dim:(B,1,H,W)
    v_spat = att_spat*v #dim:(B,C,H,W)

    att_chan = self.SpatialSim(q,k) #dim:(B,C,1,1)
    v_chan = att_chan*v #dim:(B,C,H,W)

    v_cspat = 0.5*(v_chan+v_spat)
    v_cspat = self.norm(v_cspat)

    return v_cspat #dim:(B,C,H,W)

```

Listing 3: MXNET/GLUON style pseudocode for the Relative Attention Fusion module

```

import mxnet as mx
from mxnet import nd as F
class Fusion(nn.Block):
    def __init__(self, nchannels, nheads, **kwargs):
        super().__init__(**kwargs)
        self.fuse = Conv2DN(nchannels,
                             kernel=3,
                             padding=1,
                             groups=nheads)
        self.att12 = FTAttention2D(nchannels, nheads)
        self.att21 = FTAttention2D(nchannels, nheads)

        self.gamma1 = self.params.get('gamma1',
                                       shape=(1,),
                                       init=mx.init.Zero())
        self.gamma2 = self.params.get('gamma2',
                                       shape=(1,),
                                       init=mx.init.Zero())

    def forward(self, input1, input2):
        ones = nd.ones_like(input1)

        # Attention on 1, for k,v from 2
        qin = input1
        kin = input2
        vin = input2
        att12 = self.att12(qin, kin, vin)
        out12 = input1*(ones+self.gamma1*att12)

```

```

# Attention on 2, for k,v from 1
qin = input2
kin = input1
vin = input1
att21 = self.att21(qin, kin, vin)
out21 = input2*(ones+self.gamma2*att21)

out = nd.concat(out12, out21, dim=1)
out = self.fuse(out)
return out

```

### Appendix C.2. FracTAL ResNet

In this Listing, the ResBlock consists of the sequence of BatchNorm, ReLU, Conv2D, BatchNorm, ReLU, Conv2D. The normalization can change to GroupNorm for a small batch size.

Listing 4: MXNET/GLUON style pseudocode for the Residual Attention Fusion module

```

import mxnet as mx
from mxnet import nd as F
class FAttResUnit(nn.Block):
    def __init__(self, nchannels, nheads, **kwargs):
        super().__init__(**kwargs)
        # Residual Block: sequence of
        # (BN, ReLU, Conv, BN, ReLU, Conv)
        self.ResBlock = ResBlock(nchannels,
                                   kernel=3,
                                   padding=1)
        self.att = FTAttention2D(nchannels, nheads)

        self.gamma = self.params.get('gamma',
                                       shape=(1,),
                                       init=mx.init.Zero())

    def forward(self, input):
        out = self.ResBlock(input) #dim:(B,C,H,W)
        qin = input
        vin = input
        kin = input
        att = self.attention(qin, vin, kin) #dim:(B,C,H,W)
        att = self.gamma * att
        out = (input + out)*(F.ones_like(out)+att)
        return out

```

### Appendix C.3. CEECNet building blocks

In this section we provide with pseudo-code the implementation of the CEECNet V1 unit.

Listing 5: MXNET/GLUON style pseudocode for the CEECNet V1 unit.

```

import mxnet as mx
from mxnet import nd as F
class CEECNet_unit_V1(nn.Block):
    def __init__(self, nchannels, nheads, **kwargs):
        super().__init__(**kwargs)
        # Compress-Expand

```

```

self.conv1= Conv2DN(nchannels/2)
self.compr11= Conv2DN(nchannels,k=3,p=1,s=2)
self.compr12= Conv2DN(nchannels,k=3,p=1,s=1)
self.expand1= ExpandNComb(nchannels/2)

# Expand Compress
self.conv2= Conv2DN(nchannels/2)
self.expand2= Expand(nchannels/4)
self.compr21= Conv2DN(nchannels/2,k=3,p=1,s=2)
self.compr22= Conv2DN(nchannels/2,k=3,p=1,s=1)

self.collect= Conv2DN(nchannels,k=3,p=1,s=1)

self.att= FTAttention2D(nchannels,nheads)
self.ratt12= RelFTAttention2D(nchannels,nheads)
self.ratt21= RelFTAttention2D(nchannels,nheads)

self.gamma1 = self.params.get('gamma1',
                                shape=(1,),
                                init=mx.init.Zero())
self.gamma2 = self.params.get('gamma2',
                                shape=(1,),
                                init=mx.init.Zero())
self.gamma3 = self.params.get('gamma3',
                                shape=(1,),
                                init=mx.init.Zero())

def forward(self, input):
    # Compress-Expand
    out10 = self.conv1(input)
    out1 = self.compr11(out10)
    out1 = F.relu(out1)
    out1 = self.compr12(out10)
    out1 = F.relu(out1)
    out1 = self.expand1(out1,out10)
    out1 = F.relu(out1)

    # Expand-Compress
    out20 = self.conv2(input)
    out2 = self.expand2(out20)
    out2 = F.relu(out2)
    out2 = self.compr21(out2)
    out2 = F.relu(out2)
    out2 = F.concat([out2,out20],axis=1)
    out2 = self.compr22(out2)
    out2 = F.relu(out2)

    # attention
    att = self.gamma1*self.att(input)

    # relative attention 122
    qin = out1
    kin = out2
    vin = out2
    ratt12 = self.gamma2*self.ratt12(qin,kin,vin)

```

```

# relative attention 211
qin = out2
kin = out1
vin = out1
ratt21 = self.gamma3*self.ratt21(qin,kin,vin)

ones1 = F.ones_like(out10)# nchannels/2

out122= out1*(ones1+ratt12)
out211= out2*(ones1+ratt21)
out12 = F.concat([out122,out211],dim=1)
out12 = self.collect(out12)
out12 = F.relu(out12)

# Final fusion
ones2 = F.ones_like(input)
out = (input+out12)*(ones2+att)

return out

```

---

The layers Expand and ExpandNCombine are defined through Listings 6 and 7.

Listing 6: MXNET/GLUON style pseudocode for the Expand layer used in the CEECNetV1 unit.

---

```

import mxnet as mx
from mxnet import nd as F
class Expand(nn.Block):
    def __init__(self, nchannels, nheads, **kwargs):
        super().__init__(**kwargs)
        self.conv1 = Conv2DN(nchannels,k=3, p=1,
                               groups=nheads)
        self.conv2 = Conv2DN(nchannels,k=3, p=1,
                               groups=nheads)

    def forward(self, input):

        out = F.BilinearResize2D(input,
                                   scale_height=2,
                                   scale_width=2)
        out = self.conv1(out)
        out = F.relu(out)
        out = self.conv2(out)
        out = F.relu(out)
        return out

```

---

Listing 7: MXNET/GLUON style pseudocode for the ExpandNCombine layer used in the CEECNetV1 unit.

---

```

import mxnet as mx
from mxnet import nd as F
class ExpandNCombine(nn.Block):
    def __init__(self, nchannels, nheads, **kwargs):
        super().__init__(**kwargs)
        self.conv1 = Conv2DN(nchannels,k=3, p=1,
                               groups=nheads)
        self.conv2 = Conv2DN(nchannels,k=3, p=1,
                               groups=nheads)

```



```

def forward(self, input1, input2):
    # input1 has lower spatial dimensions
    out1 = F.BilinearResize2D(input1,
                              scale.height=2,
                              scale.width=2)
    out1 = self.conv1(out1)
    out1 = F.relu(out1)

    out2 = F.concat([out1, input2], dim=1)
    out2 = self.conv2(out2)
    out2 = F.relu(out2)
    return out2

```

---

#### Appendix D. Software implementation and training characteristics

The networks mantis CEECNet and FracTAL ResNet were built and trained using the MXNET deep learning library (Chen et al., 2015), under the GLUON API. Each of the models was trained with a batch size of  $\sim 256$  on 16 nodes containing 4 NVIDIA Tesla P100 GPUs each in CSIRO HPC facilities. Due to the complexity of the network, the batch size in a single GPU iteration cannot be made larger than  $\sim 4$  (per GPU). The models were trained in a distributed scheme, using the ring allreduce algorithm, and in particular it's implementation on HOROVOD (Sergeev and Balso, 2018) for the MXNET (Chen et al., 2015) deep learning library. For all models, we used the Adam (Kingma and Ba, 2014) optimizer, with momentum parameters  $(\beta_1, \beta_2) = (0.9, 0.999)$ . The learning rate was reduced by an order of magnitude whenever the validation loss stopped decreasing. Overall we reduced the learning rate 3 times. The depth of the evolving loss function was increased every time the learning rate was reduced. The depths of the  $\langle \mathcal{FT} \rangle^d$  that we used were  $d \in \{0, 10, 20, 30\}$ .